

# Tensor completion using enhanced multiple modes low-rank prior and total variation

Haijin Zeng<sup>a</sup>, Xiaozhen Xie <sup>\*a</sup>, and Jifeng Ning<sup>b</sup>

<sup>a</sup>College of Science, Northwest A&F University, Yangling 712100,  
P.R. China

<sup>b</sup>College of Information Engineering, Northwest A&F University,  
Yangling 712100, P.R. China

## Abstract

In this paper, we propose a novel model to recover a low-rank tensor by simultaneously performing double nuclear norm regularized low-rank matrix factorizations to the all-mode matricizations of the underlying tensor. An block successive upper-bound minimization algorithm is applied to solve the model. Subsequence convergence of our algorithm can be established, and our algorithm converges to the coordinate-wise minimizers in some mild conditions. Several experiments on three types of public data sets show that our algorithm can recover a variety of low-rank tensors from significantly fewer samples than the other testing tensor completion methods.

## 1 Introduction

Tensor is a generalization of vector and matrix. A vector is a first-order or one-way tensor, and a matrix is a second-order tensor. The results of matrix completion have been successfully applied in various practical fields, such as inpainting [1], denoising [2], image batch alignment [3], key-point/saliency detection [4], and affinity learning [5]. Tensor completion as a high-order extension of matrix completion has also aroused much research interest in recent years, due to higher-order tensor arises in many applications, for instance, video inpainting [6], magnetic resonance imaging (MRI) data recovery [7], 3D image reconstruction [8], high-order web link analysis, hyperspectral or multispectral data recovery [9], personalized web search [10], and seismic data reconstruction [11].

---

\*Corresponding author: xiexzh@nwafu.edu.cn

Tensor completion is to recover the higher-order tensor with missing entries. Mathematically, this kind of problem can be modeled as

$$\min \text{rank}(\mathcal{Y}), s.t., \mathcal{P}_\Omega(\mathcal{Y}) = \mathcal{F} \quad (1)$$

where  $\mathcal{Y}$  is the underlying tensor,  $\mathcal{F}$  is the observed data,  $\Omega$  denotes the index set of observed entries,  $\mathcal{P}_\Omega$  keeps the entries in  $\Omega$  and zeros out others (one can find more details of  $\mathcal{P}_\Omega$  in Section 2.3). Tensor is a high-dimensional extension of matrix, therefore, a natural processing method is to unfold or flatten the tensor into matrix, and then use the rank of the matrix to describe the low rank structure of the tensor, i.e.,

$$\min \|\mathbf{Y}\|_0, s.t., \mathcal{P}_\Omega(\mathcal{Y}) = \mathcal{F} \quad (2)$$

where  $\mathbf{Y}$  is the matricization of  $\mathcal{Y}$ . Unfortunately, (2) is generally an NP-hard problem. By relaxing the nonconvex rank function and the  $L_0$ -norm into the  $L_1$ -norm, a convex formulation can be yielded, i.e.,

$$\min \|\mathbf{Y}\|_1, s.t., \mathcal{P}_\Omega(\mathcal{Y}) = \mathcal{F} \quad (3)$$

Further, to effectively enhance the low rank of the basic results, many methods relaxed the nonconvex rank function into the nuclear norm. Then, the optimization problem (2) can be rewritten as

$$\min \|\mathbf{Y}\|_*, s.t., \mathcal{P}_\Omega(\mathcal{Y}) = \mathcal{F}, \quad (4)$$

which can be solved by using algorithm such as fixed point continuation with approximate singular value decomposition (FPCA) [12], accelerated proximal gradient algorithm (APGL) [13] or the alternating direction method [14]. Although the above models can recover the low-rank tensor, under certain conditions, they need convert high-dimensional tensor into 2-D matrices. This strategy will introduce loss of useful multiorder structure information. For instance, the spectral dimension of hyperspectral image contains imaging results of the same spatial scene in different spectral bands, there is high correlation between the discrete spectral bands [9]; video often has multiple frames of images, and there is a temporal correlation between the images of each frame [15].

Many studies [16, 17, 18, 19, 20] have proven that completion methods directly modeling tensors can achieve better results than the ones modeling the tensor' matricization. In the literature, two common low-rank tensor completion methods are low-rank tensor decomposition and tensor rank minimization. The main low-rank tensor decomposition method generally decomposes the target tensor into a combination of several sub-tensors and matrixes, to achieve the purpose of recovering a low-rank tensor from its partially observed entries. See, e.g., weighted low-rank tensor decomposition method [21], Bayes-based framework [22, 23], multi-linear graph embedding [24, 25] and tensor SVD methods [26, 27, 28]. These methods can effectively recover tensors under certain conditions, however, they are usually sensitive to a given rank, which is usually estimated based on the raw data.

The rank minimization problem is a widely studied problem, and its robustness to noisy and missing data has also been proven. Therefore, rank minimization based methods have been universally utilized in tensor completion problems. In general, they can be solved by low-rank approximation techniques as rank estimation problems in matrix case. For example, the rank of a tensor can be determined as the smallest number of rank-1 tensor components  $r$  that requires a CANDECOMP/PARAFAC (CP) decomposition [29]. Typically, the mode- $k$  rank( $r_1, \dots, r_k$ ) estimated by the Tucker decomposition is used instead of the minimum [30, 31]. Based on the matrix sparsity measurement, Liu et al. [32, 33, 34, 35] extended this kind of matrix methods to tensors, and proposed nuclear norm-based tensor sparsity, which uses low rank attributes as constraints. Similar methods are also proposed in [36, 37, 38], in which the tensor rank approximation formulations is redefined with more relaxations. This type of method can significantly reduce the deviation of rank estimation based on the tensor nuclear norm.

Among the tensor rank minimization approach, the tensor nuclear norm based on the tensor singular value decomposition (t-SVD) [39], as the tightest convex surrogate of the tensor rank, has been widely used for LR tensor approximation [28],

$$\min \|\mathcal{Y}\|_{\text{TNN}}, s.t., \mathcal{P}_\Omega(\mathcal{Y}) = \mathcal{F} \quad (5)$$

the tensor nuclear norm of a tensor  $\mathcal{A} \in \mathbb{R}^{n_1 \times n_2 \times n_3}$ , denoted as  $\|\mathcal{A}\|_{\text{TNN}}$ , is defined as the average of the nuclear norm of all the frontal slices of  $\mathcal{A}$ , i.e.,  $\|\mathcal{A}\|_{\text{TNN}} := \frac{1}{n_3} \sum_{i=1}^{n_3} \|\bar{\mathcal{A}}^{(i)}\|_*$ .

Further, based on TNN, Jiang et al. [40] proposed a partial sum of the tubal nuclear norm (PSTNN) of a tensor, which is a surrogate of the tensor tubal multi-rank. The PSTNN of a three way tensor  $\mathcal{A} \in \mathbb{R}^{n_1 \times n_2 \times n_3}$  is given as:  $\|\mathcal{A}\|_{\text{PSTNN}} = \sum_{i=1}^{n_3} \|\hat{\mathcal{A}}^{(i)}\|_{p=N}$ . Then, the model of LR tensor completion can be written as

$$\min \|\mathcal{Y}\|_{\text{PSTNN}}, s.t., \mathcal{P}_\Omega(\mathcal{Y}) = \mathcal{F} \quad (6)$$

In (6),  $\|\cdot\|_{p=N}$  is defined as  $\|\mathbf{X}\|_{p=N} = \sum_{i=N+1}^{\min(n_1, n_2)} \sigma_i(\mathbf{X})$  for a matrix  $\mathbf{X} \in \mathbb{C}^{n_1 \times n_2}$ , where  $\sigma_i(\mathbf{X}) (i = 1, \dots, \min(n_1, n_2))$  denotes its  $i$ -th largest singular value. However, the methods for TC in [28, 40] need to compute the singular value decomposition (SVD), which become very slow or even not applicable for large-scale problems [41].

For LRTC, such conventional methods are useful but only to a certain extent. Firstly, conventional approaches utilized only the sparsity prior along each mode independently. This limits the use of prior knowledge of close multilinear interactions among multiple dimensions of a given tensor object. one can see an example in Fig. 1, as presented in Fig. 1, the three modes of tensors have similar low-rank property. Secondly, the affinity matrices in [30, 31, 29, 40] is constructed based on the raw data. However there may exist noise and outlier in the raw data, e.g. video images variations caused by illumination. These factors

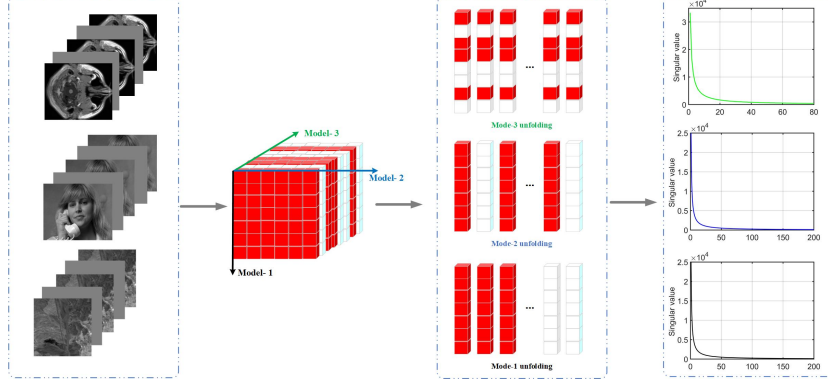


Figure 1: Low rank properties of tensor mode- $n$  unfoldings

would reduce the ability to represent the correlation among data. Thirdly, all these methods adopt single nuclear norm or partial sum minimization of singular values norm, which would cause suboptimal solution of the low rank based problem.

To tackle these difficulties, motivated and convinced by the results [42, 41] that utilizing all mode low-ranknesses of the tensor gives much better performance, for a tensor  $\mathcal{Y} \in \mathbb{R}^{n_1 \times n_2 \times n_3}$ , we could formulate a double nuclear norm based low rank representation model on low-rank tensor completion. Specifically, we first apply parallel low-rank matrix factorization to each mode unfolding of the tensor. Then, as the model structure is implicitly included in the low-rank factorization model, according to the factor priors, which are usually known a priori in real-world tensor objects, we add the double nuclear norm regularization to the factor matrix obtained by the decomposition, to characterize the underlying joint-manifold drawn from the model factors. By exploiting this auxiliary information, our method leverages two classic schemes and accurately estimates the model factors and missing entries. The proposed model-1, named low-rank tensor completion by bilinear mode matrix factorization (BMF-LRTC), is formulated as

$$\begin{aligned} \min \sum_{n=1}^N (\tau_n \|\mathbf{X}_n\|_* + \lambda_n \|\mathbf{A}_n\|_*), \\ s.t., \quad \mathbf{Y}_{(n)} = \mathbf{A}_n \mathbf{X}_n, n = 1, 2, 3, \dots, N; \quad \mathcal{P}_\Omega(\mathcal{Y}) = \mathcal{F} \end{aligned} \quad (7)$$

Further, to consider the inner geometry or structure of data space, we integrated the the total variation (TV) regularization to construct the global relationship of data, and propose our model-2, named TV regularized bilinear mode matrix factorization model for low-rank tensor completion (TVB-LRTC),

$$\begin{aligned} \min \sum_{n=1}^N (\tau_n \|\mathbf{X}_n\|_* + \lambda_n \|\mathbf{A}_n\|_*) + \mu \|\mathbf{X}_3\|_{\text{TV}}, \\ \text{s.t.}, \quad \mathbf{Y}_{(n)} = \mathbf{A}_n \mathbf{X}_n, n = 1, 2, 3, \dots, N, \quad \mathcal{P}_\Omega(\mathcal{Y}) = \mathcal{F} \end{aligned} \quad (8)$$

where  $\mathbf{A}_n$  represents a library (each column contains a signature of the  $n$ -th mode direction), and  $\mathbf{X}_n$  is called an encoding. For example, in the unmixing problem for hyperspectral image [43], each column of  $\mathbf{A}_3$  contains a spectral signature, and each row of  $\mathbf{X}_3$  contains the fractional abundances of a given endmember. This interpretation is also valid for the mode-3 unfolding of video and MRI. It is worth noting that the proposed model can fully capture all mode low-ranknesses and piecewise smooth prior of the underlying tensor, and thus is expected to have a strong ability of low-rank tensor completion. For the other details of the model, we ask for the readers patience until Section 3.

## 2 Preliminary

Before introducing our model and algorithm, we review some notations, tensor operations, regularizers with physical meaning and operators.

### 2.1 Notations

Following [41], vectors are denoted as bold lower-case letters  $\mathbf{x}, \mathbf{y}, \dots$ , matrices are denoted as bold upper-case letters  $\mathbf{X}, \mathbf{Y}, \dots$ , and tensors are denoted as caligraphic letters  $\mathcal{X}, \mathcal{Y}, \dots$ . Let  $x_{i_1 \dots i_N}$  represents the  $(i_1, \dots, i_N)$ -th component of an  $N$ -way tensor  $\mathcal{X}$ , then, for  $\mathcal{X}, \mathcal{Y} \in \mathbb{R}^{I_1 \times \dots \times I_N}$ , their inner product is defined as

$$\langle \mathcal{X}, \mathcal{Y} \rangle = \sum_{i_1=1}^{I_1} \dots \sum_{i_N=1}^{I_N} x_{i_1 \dots i_N} y_{i_1 \dots i_N}. \quad (9)$$

Based on the inner product, one can define the **Frobenius norm** of a tensor  $\mathcal{X}$  as  $\|\mathcal{X}\|_F = \sqrt{\langle \mathcal{X}, \mathcal{X} \rangle}$ . **Fibers** of tensor  $\mathcal{X}$  are defined as a vector obtained by fixing all indices of  $\mathcal{X}$  except one, and **slices** of  $\mathcal{X}$  are defined as a matrix by fixing all indices of  $\mathcal{X}$  except two. The **mode- $n$  matricization/unfolding** of  $\mathcal{X} \in \mathbb{R}^{I_1 \times \dots \times I_N}$  is denoted as a matrix  $\mathbf{X}_{(n)} \in \mathbb{R}^{I_n \times \prod_{j \neq n} I_j}$  with columns being the mode- $n$  fibers of  $\mathcal{X}$  in the lexicographical order.

Furthermore, to clearly represent the matricization process, we define **unfold <sub>$n$</sub>** ( $\mathcal{X}$ ) =  $\mathbf{X}_{(n)}$ , **fold <sub>$n$</sub>**  is the inverse of **unfold <sub>$n$</sub>** , i.e., **fold <sub>$n$</sub>** (**unfold <sub>$n$</sub>** ( $\mathcal{X}$ )) =  $\mathcal{X}$ . The  $n$ -rank of an  $N$ -way tensor  $\mathcal{X}$ , denoted as  $\text{rank}_n(\mathcal{X})$ , is the rank of  $\mathbf{X}_{(n)}$ , and the rank of  $\mathcal{X}$  is defined as an array:  $\text{rank}(\mathcal{X}) = (\text{rank}(\mathbf{X}_{(1)}), \dots, \text{rank}(\mathbf{X}_{(N)}))$ .

### 2.2 Total variation

The isotropic **total variation (TV)** is defined as follows:

$$\|\mathbf{X}_3\|_{\text{TV}} := \sum_{k=1}^S \sum_{i=1}^{r_n} \sum_{j=1}^{n_2} \sqrt{\left| \tilde{\mathbf{D}}_{j,1} \mathbf{X}_3^{(i,k)} \right|^2 + \left| \tilde{\mathbf{D}}_{j,2} \mathbf{X}_3^{(i,k)} \right|^2} \quad (10)$$

where  $\mathbf{X}_3^{(i,k)}$  represents the  $k$ -th block of  $i$ -th row of  $\mathbf{X}_3$ ,  $\tilde{\mathbf{D}}_{j,1}$  and  $\tilde{\mathbf{D}}_{j,2}$  represent the discrete gradient operators at the 1st- and 2nd- mode directions, respectively. Following the representation of  $\tilde{\mathbf{D}}$ ,  $\tilde{\mathbf{D}}_{j,1} \mathbf{X}_3^{(i,k)}$  denotes the gradient values of  $\mathbf{X}_3^{(i,k)}$  at the 1st mode directions and  $\tilde{\mathbf{D}}_{j,2} \mathbf{X}_3^{(i,k)}$  denotes the gradient values of  $\mathbf{X}_3^{(i,k)}$  at the 2nd mode directions of the  $j$ -th pixel in  $\mathbf{X}_3^{(i,k)}$ .

### 2.3 Operators

The **Proximal Operator** of a given convex function  $f(x)$  is defined as

$$\text{prox}_f(y) := \arg \min_x f(x) + \frac{\rho}{2} \|x - y\|^2 \quad (11)$$

where  $\rho$  is a positive constant. Friendly, the problem  $\min_x \{f(x)\}$  is equivalent to  $\min_{x,y} \{f(x) + \frac{\rho}{2} \|x - y\|^2\}$ . Thus, the minimization of  $\{f(x)\}$  can be solved by iteratively solving  $\text{prox}_f(x^k)$ , where  $x^k$  denotes the latest update of  $x$ . The highlight of the proximal operator is that it can guarantee the strong convexity of objective function (11), as long as  $f(x)$  is convex.

Let  $\Omega$  be the index set of observed entries, then  $\mathcal{P}_\Omega$  keeps the entries in  $\Omega$  and zeros out others, i.e.,

$$(\mathcal{P}_\Omega(\mathcal{Y}))_{i_1 \dots i_n} = \begin{cases} y_{i_1, \dots, i_n}, & (i_1, \dots, i_n) \in \Omega \\ 0, & \text{otherwise} \end{cases} \quad (12)$$

## 3 Proposed model and algorithm

### 3.1 Proposed model

The objective function of our model-1 (7) is as following:

$$f(\mathbf{X}, \mathbf{A}, \mathcal{Y}) = \min \sum_{n=1}^N \left( \frac{\alpha_n}{2} \|\mathbf{Y}_{(n)} - \mathbf{A}_n \mathbf{X}_n\|_{\text{F}}^2 + \tau_n \|\mathbf{X}_n\|_* + \lambda_n \|\mathbf{A}_n\|_* \right) \quad (13)$$

The objective function of our model-2 (8) is as following:

$$f(\mathbf{X}, \mathbf{A}, \mathcal{Y}) = \min \sum_{n=1}^N \left( \frac{\alpha_n}{2} \|\mathbf{Y}_{(n)} - \mathbf{A}_n \mathbf{X}_n\|_{\text{F}}^2 + \tau_n \|\mathbf{X}_n\|_* + \lambda_n \|\mathbf{A}_n\|_* \right) + \mu \|\mathbf{X}_3\|_{\text{TV}} \quad (14)$$

We first explain the reason why we adopt the low-rank regularization to  $\mathbf{A}_n$  and  $\mathbf{X}_n$ , which represented by the double nuclear norm. In an  $n$ th-order

tensor, each order represents one factor and has its specific inherent structural properties. Therefore, each mode of the underlying tensor has specific prior information. Although a tensor could be comprised of randomly arranged elements, it is usually assumed that the withinfactor and joint-factor variations are known a priori and can be regarded as auxiliary information [25]. For example, a video object is a third-order tensor with variations spanned by the rows, columns, and time axis. Even when the value of an element is unknown, we may reasonably infer that adjacent rows/columns/frames are highly correlated. This is because the local similarity of visual data usually exists in within-factor relations (e.g., between adjacent rows/ columns/frames) or joint-factor relations (e.g., between spatially adjacent and temporally adjacent pixels). See Fig. 1 for an illustration. As shown in the singular value curve of  $\mathbf{Y}_{(n)}$ , ( $n = 1, 2, 3$ ), in Fig. 1, it is obviously seen that the singular value curves of  $\mathbf{Y}_{(1)}$ ,  $\mathbf{Y}_{(2)}$  and  $\mathbf{Y}_{(3)}$  decay rapidly, that is to say that only a small part of the singular values are greater than zero. Therefore, the three modes of the tensor data have the similar low-rank property. Actually, this phenomenon has specific physical meaning. For instance, in hyperspectral image context, it is well known that each spectral characteristic can be represented by a linear combination of a small number of pure spectral endmembers. It means that the mode-3 matrix  $\mathbf{Y}_{(3)}$  of a clean HSI  $\mathcal{Y} \in \mathbb{R}^{m \times n \times p}$  can be decomposed into  $\mathbf{Y}_{(3)} = \mathbf{A}_3 \mathbf{X}_3$ , where  $\mathbf{X}_3 \in \mathbb{R}^{r \times p}$  is the so-called endmember matrix, and  $\mathbf{A}_3 \in \mathbb{R}^{mn \times r}$  is regarded as the abundance matrix. As described in [44], the number of endmembers  $r$  is relatively small, i.e.,  $r \ll p$  or  $r \ll mn$ . That is to say that only a small part of the singular values are greater than zero, as shown in the fourth column of Fig. 1. Based on the above facts, to utilize all mode low-ranknesses of the tensor to gives much better performance, we use low rank regularizers to explore the multiple modal low-rank prior of the underlying tensor, which has practical physical meaning.

To effectively explore the inherent low-rank prior knowledge of the tensor without increasing time and memory consumption, instead of the traditional single nuclear norm or decomposition, we first apply low-rank matrix factorization to each mode unfolding of the tensor [41]. Then, as the model structure is implicitly included in the low-rank factorization model, according to the factor priors, which are usually known a priori in real-world tensor objects, we add the double nuclear norm regularization to the factor matrix obtained by the decomposition, to characterize the underlying joint-manifold drawn from the model factors. By exploiting this auxiliary information, our method leverages two classic schemes and accurately estimates the model factors and missing entries. However, it is difficult to directly calculate the nuclear norm of the product of two matrices, i.e.,  $\|\mathbf{Y}_{(n)}\|_* = \|\mathbf{A}_n\|_* \|\mathbf{X}_n\|_*$ ,  $n = 1, 2, 3, \dots, N$ , in order to reduce the computational complexity of the model, we simplified the dual nuclear norm. Specifically, according to the fundamental inequality, we have

$$\begin{aligned}
\min \|\mathbf{Y}_{(n)}\|_* &= \min_{\mathbf{Y}_{(n)}=\mathbf{A}_n \mathbf{X}_n} \|\mathbf{A}_n\|_* \|\mathbf{X}_n\|_* \\
&= \min_{\mathbf{Y}_{(n)}=\mathbf{A}_n \mathbf{X}_n} \left( \frac{1}{2} (\|\mathbf{A}_n\|_* + \|\mathbf{X}_n\|_*) \right)^2, n = 1, 2, 3, \dots, N.
\end{aligned} \tag{15}$$

Then, we explain why we integrated the the TV regularization of  $\mathbf{X}_3$  to the proposed low-rank tensor completion model. The TV regularization measures the difference between a pixel and its neighbors. The smaller the difference is, the better the TV regularization plays. Because the data is piecewise smooth with respect to the 1st- and 2nd-mode direction, the difference between the pixel of  $\mathbf{X}_n$  and its 1st- and 2nd-mode direction neighbors is small. Thus, we can introduce the TV regularization of  $\mathbf{X}_n$  at the 1st-and 2nd-mode direction into the tensor completion problem. However,  $\mathbf{X}_1$  and  $\mathbf{X}_2$  do not contain the complete information of the 1st- and 2nd mode for  $\mathcal{Y}$ , because the rank of  $\mathbf{Y}_{(1)}$  is  $r_1$  ( $r_1 < I_1$ ), that is, the dimension of the corresponding tensor is  $r_1 \times I_2 \times \dots \times I_N$  [45]. Thus, we introduce the TV regularization of  $\mathbf{X}_{n_0}, n_0 \in \{3, 4, \dots, N\}$ . Without loss of generality, we adopt the TV regularization of  $\mathbf{X}_3$ .

### 3.2 Proposed algorithm

The proposed model-1 and model-2 are two complicated optimization problems, which are difficult to solve directly. Here, we adopt the block successive upper-bound minimization (BSUM)[46] to solve them.

According to the proximal operator, the update can be written as as:

$$p(S, S^k) = f(\mathbf{X}, \mathbf{A}^k, \mathcal{Y}^k) + \frac{\rho}{2} \|\mathbf{X} - \mathbf{X}^k\|_F^2 \tag{16}$$

where  $\rho > 0$  is the proximal parameter,  $S = (\mathbf{X}, \mathbf{A}, \mathcal{Y})$  and  $S^k = (\mathbf{X}^k, \mathbf{A}^k, \mathcal{Y}^k)$ . Let

$$\begin{cases} g_1(\mathbf{X}, S_1^k) = f(\mathbf{X}, \mathbf{A}^k, \mathcal{Y}^k) + \frac{\rho}{2} \|\mathbf{X} - \mathbf{X}^k\|_F^2 \\ g_2(\mathbf{A}, S_2^k) = f(\mathbf{X}^{k+1}, \mathbf{A}, \mathcal{Y}^k) + \frac{\rho}{2} \|\mathbf{A} - \mathbf{A}^k\|_F^2 \\ g_3(\mathcal{Y}, S_3^k) = f(\mathbf{X}^{k+1}, \mathbf{A}^{k+1}, \mathcal{Y}) + \frac{\rho}{2} \|\mathcal{Y} - \mathcal{Y}^k\|_F^2 \end{cases} \tag{17}$$

and  $S_1^k = (\mathbf{X}^k, \mathbf{A}^k, \mathcal{Y}^k)$ ,  $S_2^k = (\mathbf{X}^{k+1}, \mathbf{A}^k, \mathcal{Y}^k)$ ,  $S_3^k = (\mathbf{X}^{k+1}, \mathbf{A}^{k+1}, \mathcal{Y}^k)$ . Then, problem (16) can be rewritten as follows

$$\begin{cases} \mathbf{X}^{k+1} = \operatorname{argmin}_{\mathbf{X}} g_1(\mathbf{X}, S_1^k) \\ \mathbf{A}^{k+1} = \operatorname{argmin}_{\mathbf{A}} g_2(\mathbf{A}, S_2^k) \\ \mathcal{Y}^{k+1} = \operatorname{argmin}_{\mathcal{Y} \in \mathcal{F}} g_3(\mathcal{Y}, S_3^k) \end{cases} \tag{18}$$

#### 3.2.1 Update $\mathbf{X}_n$ with fixing others

The  $X_n$ -sub-problem, which can be written as follows



$$\begin{aligned} \mathbf{X}_n^{k+1} = \operatorname{argmin} \sum_{n=1}^N & \left( \frac{\alpha_n}{2} \|\mathbf{Y}_{(n)} - \mathbf{A}_n \mathbf{X}_n\|_{\mathbf{F}}^2 + \tau_n \|\mathbf{X}_n\|_* \right. \\ & \left. + \frac{\rho_n}{2} \|\mathbf{X}_n - \mathbf{X}_n^k\|_{\mathbf{F}}^2 \right) + \mu \|\mathbf{X}_3\|_{\text{TV}} \end{aligned} \quad (19)$$

To efficiently solve the proposed model denoising model, we first introduce two auxiliary variables. Then (19) can be rewritten as

$$\begin{aligned} \operatorname{argmin}_{\mathbf{X}_n, \mathbf{Z}_n} \sum_{n=1}^N & \left( \frac{\alpha_n}{2} \|\mathbf{Y}_{(n)} - \mathbf{A}_n \mathbf{X}_n\|_{\mathbf{F}}^2 + \tau_n \|\mathbf{Z}_n\|_* + \frac{\rho_n}{2} \|\mathbf{X}_n - \mathbf{X}_n^k\|_{\mathbf{F}}^2 \right) \\ & + \mu \|\mathbf{X}_3\|_{\text{TV}}, \text{ s.t., } \mathbf{X}_n = \mathbf{Z}_n, \mathcal{P}_{\Omega}(\mathcal{Y}) = \mathcal{F} \end{aligned} \quad (20)$$

Based on the ALM method, the above minimization problem (20) can be transformed into minimizing the following augmented Lagrangian function:

$$\begin{aligned} L(\mathbf{X}, \mathbf{Z}, \Gamma_n^{\mathbf{X}}) = \min \sum_{n=1}^N & \left( \frac{\alpha_n}{2} \|\mathbf{Y}_{(n)} - \mathbf{A}_n \mathbf{X}_n\|_{\mathbf{F}}^2 + \tau_n \|\mathbf{Z}_n\|_* + \frac{\rho_n}{2} \|\mathbf{X}_n - \mathbf{X}_n^k\|_{\mathbf{F}}^2 \right. \\ & \left. + \langle \Gamma_n^{\mathbf{X}}, \mathbf{X}_n - \mathbf{Z}_n \rangle + \frac{\rho_n}{2} \|\mathbf{X}_n - \mathbf{Z}_n\|_{\mathbf{F}}^2 \right) + \mu \|\mathbf{X}_3\|_{\text{TV}}, \\ & \text{s.t., } \mathcal{P}_{\Omega}(\mathcal{Y}) = \mathcal{F} \end{aligned} \quad (21)$$

With others fixed, the minimization subproblem for  $\mathbf{Z}_n$  can be deduced from (21) as following

$$\mathbf{Z}_n^{k+1} = \operatorname{argmin}_{\mathbf{Z}_n} \tau_n \|\mathbf{Z}_n\|_* + \frac{\rho_n}{2} \|\mathbf{X}_n^k - \mathbf{Z}_n + \Gamma_n^{\mathbf{X}} / \rho_n\|_{\mathbf{F}}^2 \quad (22)$$

**Lemma 1** [47]: Supposing  $\mathbf{M}$  is a matrix of size  $I_1 I_2 \times I_3$ , and the singular value of matrix  $\mathbf{M}$  of rank  $r$  is decomposed into

$$\mathbf{M} = \mathbf{P} \mathbf{E}_r \mathbf{Q}^*, \mathbf{E}_r = \operatorname{diag} \left( \{\sigma_i\}_{1 \leq i \leq r} \right)$$

The singular value shrinkage operator then obeys

$$\operatorname{SH}_{\delta}(\mathbf{M}) = \arg \min_{\operatorname{rank}(\mathbf{X}) \leq r} \delta \|\mathbf{X}\|_* + \frac{1}{2} \|\mathbf{X} - \mathbf{W}\|_{\mathbf{F}}^2,$$

where

$$\operatorname{SH}_{\delta}(\mathbf{W}) = \mathbf{P} \operatorname{diag} \{ \max((\sigma_i - \delta), 0) \} \mathbf{Q}^*. \quad (23)$$

By using **Lemma 1**, it is easy to get

$$\mathbf{Z}_n^{k+1} = \operatorname{SH}_{\frac{\tau_n}{\rho_n}}(\mathbf{X}_n^k + \Gamma_n^{\mathbf{X}} / \rho_n), n = 1, 2, 3, 4, \dots, N \quad (24)$$

Based on the ADM algorithm, the multipliers are updated by the following equations:

$$\Gamma_n^{\mathbf{X}} = \Gamma_n^{\mathbf{X}} + \mathbf{X}_n - \mathbf{Z}_n \quad (25)$$

In the following, we first solve the optimization problem of  $\mathbf{X}_n (n \neq 3)$ , which is relatively simple, and then use ADM to solve the optimization problem of  $\mathbf{X}_3$ . With others fixed, the minimization subproblem for  $\mathbf{X}_n (n \neq 3)$  can be deduced from (21) as following

$$\begin{aligned} \mathbf{X}_n^{k+1} = \operatorname{argmin}_{\mathbf{X}_n} \frac{\alpha_n}{2} \|\mathbf{Y}_{(n)} - \mathbf{A}_n^k \mathbf{X}_n\|_{\mathbf{F}}^2 + \rho_n \left\| \mathbf{X}_n - \frac{\mathbf{Z}_n^{k+1} - \Gamma_n^k / \mu_n + \mathbf{X}_n^k}{2} \right\|_{\mathbf{F}}^2 \\ , n = 1, 2, 4, \dots, N \end{aligned} \quad (26)$$

the minimization subproblem (26) of  $\mathbf{X}_n^{k+1} (n = 1, 2, 4, \dots, N)$  is a convex function, which has the following closed-form solution

$$\begin{aligned} \mathbf{X}_n^{k+1} = (\alpha_n \mathbf{A}_n^T \mathbf{A}_n + 2\rho \mathbf{I}_n)^{-1} [\alpha_n \mathbf{A}_n^T \mathbf{Y}_{(n)} + \mu_n (\frac{\mathbf{Z}_n^{k+1} - \Gamma_n^k / \mu_n + \mathbf{X}_n^k}{2})], \\ n = 1, 2, 4, \dots, N \end{aligned} \quad (27)$$

Compared with the optimization problem of  $X_n, n = 1, 2, 4, \dots, N$ , the optimization problem of  $X_3$  has an additional TV regular term imposed on  $X_3$ , i.e.,

$$\begin{aligned} \mathbf{X}_3^{k+1} = \operatorname{argmin}_{\mathbf{X}_3} \frac{\alpha_3}{2} \|\mathbf{Y}_{(3)} - \mathbf{A}_3^k \mathbf{X}_3\|_{\mathbf{F}}^2 + \rho_3 \left\| \mathbf{X}_3 - \frac{\mathbf{Z}_3^{k+1} - \Gamma_3^k / \mu_3 + \mathbf{X}_3^k}{2} \right\|_{\mathbf{F}}^2 \\ + \mu \|\mathbf{X}_3\|_{\text{TV}} \end{aligned} \quad (28)$$

The problem of  $\mathbf{X}_3$  can be solved efficiently using using ADMM [48, 49, 45]. To obtain the closed solution of  $\mathbf{X}_3$ , we transpose (28), and then solving (28) is equivalent to solving the following problems,

$$\min_{\mathbf{X}_3} \frac{1}{2} \left\| \hat{\mathbf{Y}}_{(3)}^k - \hat{\mathbf{X}}_3 \hat{\mathbf{A}}_3^k \right\|_{\mathbf{F}}^2 + \frac{\rho}{2} \left\| \hat{\mathbf{X}}_3 - \frac{\hat{\mathbf{Z}}_3^{k+1} - \hat{\Gamma}_3^k / \mu_3 + \hat{\mathbf{X}}_3^k}{2} \right\|_{\mathbf{F}}^2 + \mu \|\hat{\mathbf{X}}_3\|_{\text{TV}} \quad (29)$$

where  $\rho = \frac{\rho_3}{\alpha_3}$ ,  $\hat{\mathbf{X}}$  represents the transpose of  $\mathbf{X}$ . For simplicity, let  $\hat{\mathbf{X}}_3^k = \frac{\hat{\mathbf{Z}}_3^{k+1} - \hat{\Gamma}_3^k / \mu_3 + \hat{\mathbf{X}}_3^k}{2}$ , then, according to ADM, (29) can be rewritten as

$$\begin{aligned} \min_{\hat{\mathbf{X}}_3, \mathbf{U}} \mu \sum_{i=1}^{s_3} \sum_{j=1}^{r_3} \|\mathbf{U}_{i,j}\|_2 + \frac{1}{2} \left\| \hat{\mathbf{Y}}_{(3)}^k - \hat{\mathbf{X}}_3 \hat{\mathbf{A}}_1^k \right\|_{\mathbf{F}}^2 + \frac{\rho}{2} \left\| \hat{\mathbf{X}}_3 - \hat{\mathbf{X}}_3^k \right\|_{\mathbf{F}}^2 \\ s.t. \quad \mathbf{U}_1 = \mathbf{D}_1 \hat{\mathbf{X}}_3, \mathbf{U}_2 = \mathbf{D}_2 \hat{\mathbf{X}}_3 \end{aligned} \quad (30)$$

where  $\mathbf{U}_{i,j} = [(\mathbf{U}_1)_{i,j}, (\mathbf{U}_2)_{i,j}] \in \mathbb{R}^{1 \times 2}$ ,  $(\mathbf{U}_1)_{i,j}$  and  $(\mathbf{U}_2)_{i,j}$  denote the  $(i, j)$  th entries of  $\mathbf{U}_1$  and  $\mathbf{U}_2$ , respectively;  $\mathbf{D}_i := \text{Diag}(\tilde{\mathbf{D}}_i, \tilde{\mathbf{D}}_i, \dots, \tilde{\mathbf{D}}_i)$ , specifically,  $i = 1, 2$ , and  $\mathbf{D}_1$  and  $\mathbf{D}_2$  are the assembled first-order difference matrices in the 1 st-and 2 nd-mode directions based on  $\tilde{\mathbf{D}}_{j,1}$  and  $\tilde{\mathbf{D}}_{j,2}$ , respectively, in (10). where  $I_{i \times i}$  is the  $i$ -by- $i$  identity matrix. The problem (30) can be solved by solving two decoupled subproblems, which the convergence can be guaranteed [50]. The augmented Lagrangian function of (30) is

$$L(\hat{\mathbf{X}}_3, \mathbf{U}, \Lambda) = \frac{1}{2} \left\| \hat{\mathbf{Y}}_{(3)}^k - \hat{\mathbf{X}}_3 \hat{\mathbf{A}}_3^k \right\|_{\text{F}}^2 + \frac{\rho}{2} \left\| \hat{\mathbf{X}}_3 - \hat{\mathbf{X}}_3^k \right\|_{\text{F}}^2 + \mu \sum_{i=1}^{s_3} \sum_{j=1}^{r_3} \|\mathbf{U}_{ij}\|_2 \\ + \left\langle \Lambda, \mathbf{B} \hat{\mathbf{X}}_3 + \mathbf{C} \mathbf{U} \right\rangle + \frac{\beta}{2} \left\| \beta \hat{\mathbf{X}}_3 + \mathbf{C} \mathbf{U} \right\|_{\text{F}}^2 \quad (31)$$

where  $\mathbf{B} \hat{\mathbf{X}}_3 + \mathbf{C} \mathbf{U} := [\mathbf{D}_1 \quad \mathbf{D}_2]^T \hat{\mathbf{X}}_3 - \hat{\mathbf{I}}_{2s_3 \times 2s_3} [\mathbf{U}_1 \quad \mathbf{U}_2]^T = \mathbf{0}_{2s_3 \times r_3}$  is a convenient form of the constraints in (30);  $\Lambda = (\Lambda_1, \Lambda_2)^T$ , and  $\beta > 0$  is the penalty parameter. Then, (31) can be solved by alternately iterating the three variables  $\hat{\mathbf{X}}_3$ ,  $\mathbf{U}$  and  $\Lambda$ . Specifically, let  $p$  denotes the iteration indicator for solving the problem (30), with others fixed, for the  $\mathbf{X}_3$ -subproblem, we have

$$\hat{\mathbf{X}}_3^{k+1,p+1} \in \text{argmin} \left\{ \frac{1}{2} \left\| \hat{\mathbf{Y}}_{(3)}^k - \hat{\mathbf{X}}_3 \hat{\mathbf{A}}_3^k \right\|_{\text{F}}^2 + \frac{\rho}{2} \left\| \hat{\mathbf{X}}_3 - \hat{\mathbf{X}}_3^k \right\|_{\text{F}}^2 \right. \\ \left. + \left\langle \Lambda^p, \mathbf{B} \hat{\mathbf{X}}_3 + \mathbf{C} \mathbf{U}^p \right\rangle + \frac{\beta}{2} \left\| \mathbf{B} \hat{\mathbf{X}}_3 + \mathbf{C} \mathbf{U}^p \right\|_{\text{F}}^2 \right\} \quad (32)$$

then, the solution of (32) can be obtained by using the classical Sylvester matrix equation

$$\hat{\mathbf{X}}_3 (\hat{\mathbf{A}}_3^k (\hat{\mathbf{A}}_3^k)^T) + \beta \mathbf{B}^T \mathbf{B} \hat{\mathbf{X}}_3 + \rho \hat{\mathbf{X}}_3 = \rho \hat{\mathbf{X}}_3^k + \hat{\mathbf{Y}}_{(3)}^k (\hat{\mathbf{A}}_3^k)^T - \mathbf{B}^T \Lambda^p - \beta \mathbf{B}^T \mathbf{C} \mathbf{U}^p \quad (33)$$

By using the Kronecker product notations, (33) can be rewritten as:

$$\left( \hat{\mathbf{A}}_3^k (\hat{\mathbf{A}}_3^k)^T \otimes \mathbf{I} + \beta \mathbf{I} \otimes \mathbf{B}^T \mathbf{B} + \rho \mathbf{I} \otimes \mathbf{I} \right) \text{vec}(\hat{\mathbf{X}}_3) \\ = \text{vec} \left( \rho \hat{\mathbf{X}}_3^k + \hat{\mathbf{Y}}_{(3)}^k (\hat{\mathbf{A}}_3^k)^T - \mathbf{B}^T \Lambda^p - \beta \mathbf{B}^T \mathbf{C} \mathbf{U}^p \right) \quad (34)$$

where  $\text{vex}(\cdot)$  refers to a vector by lexicographical ordering of the entries in a matrix. Using singular value decomposition of  $\hat{\mathbf{A}}_3^k$  and the Fourier decomposition of  $\mathbf{B}^T \mathbf{B}$  with periodic boundary condition:  $\hat{\mathbf{A}}_3^k = \mathbf{P} \Sigma \mathbf{Q}^*$ ,  $\mathbf{B}^T \mathbf{B} = \mathbf{F}^* \Psi^2 \mathbf{F}$ , we can solve the problem (34) efficiently. Then, (34) can be rewritten as:

$$(\mathbf{P} \otimes \mathbf{F}^*) \left( \Sigma^2 \otimes \mathbf{I} + \beta \mathbf{I} \otimes \Psi^2 + \rho \mathbf{I} \otimes \mathbf{I} (\mathbf{P}^* \otimes \mathbf{F}) \right) \text{vec}(\hat{\mathbf{X}}_3) \\ = \text{vec} \left( \rho \hat{\mathbf{X}}_3^k + \hat{\mathbf{Y}}_{(3)}^k (\hat{\mathbf{A}}_3^k)^T - \mathbf{B}^T \Lambda^p - \beta \mathbf{B}^T \mathbf{C} \mathbf{U}^p \right) \quad (35)$$

the solution  $\text{vec}(\hat{\mathbf{X}}_3)$  is explicitly expressed as:

$$\begin{aligned} \text{vec}(\hat{\mathbf{X}}_3) &= (\mathbf{P} \otimes \mathbf{F}^*) (\Sigma^2 \otimes \mathbf{I} + \beta \mathbf{I} \otimes \Psi^2 + \rho \mathbf{I} \otimes \mathbf{I})^{-1} (\mathbf{P}^* \otimes \mathbf{F}) \\ &\quad \cdot \text{vec} \left( \rho \hat{\mathbf{X}}_3^* + \hat{\mathbf{Y}}_{(3)}^k (\hat{\mathbf{X}}_3^*)^T - \mathbf{B}^T \Lambda^P - \beta \mathbf{B}^T \mathbf{C} \mathbf{U}^P \right) \end{aligned} \quad (36)$$

With others fixed, the minimization subproblem for  $\mathbf{U}$  can be deduced from (31) as following:

$$\mathbf{U}^{p+1} = \underset{\mathbf{U}}{\text{argmin}} \mu \sum_{i=1}^{s_3} \sum_{j=1}^{r_3} \|\mathbf{U}_{i,j}\|_2 + \frac{\beta}{2} \left\| \mathbf{B} \hat{\mathbf{X}}_3^{k+1,p+1} + \mathbf{C} \mathbf{U} + \frac{\Lambda^p}{\beta} \right\|_{\mathbf{F}}^2 \quad (37)$$

the solution of (37) can be transformed into solving  $s_3 r_3$  two-variable minimization problems independently:

$$\begin{aligned} \min \mu &\sqrt{\left| (\mathbf{U}_1)_{i,j} \right|^2 + \left| (\mathbf{U}_2)_{i,j} \right|^2} + \frac{\beta}{2} \left[ (\mathbf{U}_1)_{i,j} - \left( \mathbf{D}_1 \hat{\mathbf{X}}_3^{k+1,p+1} \right)_{i,j} - \frac{1}{\beta} (\Lambda_1^p)_{i,j} \right]^2 \\ &+ \frac{\beta}{2} \left[ (\mathbf{U}_2)_{i,j} - \left( \mathbf{D}_2 \hat{\mathbf{X}}_3^{k+1,p+1} \right)_{i,j} - \frac{1}{\beta} (\Lambda_2^p)_{i,j} \right]^2, \end{aligned} \quad (38)$$

whose solution can be obtained by using the well-known 2-D shrinkage formula,

$$\left[ (\mathbf{U}_1)_{i,j}, (\mathbf{U}_2)_{i,j} \right] = \max \left\{ \|\mathbf{T}_{i,j}\|_2 - \frac{\mu}{\beta}, 0 \right\} \frac{\mathbf{T}_{i,j}}{\|\mathbf{T}_{i,j}\|_2}, 1 \leq i \leq s_3, 1 \leq j \leq r_3 \quad (39)$$

where  $\mathbf{T}_{i,j} = \left[ \left( \mathbf{D}_1 \hat{\mathbf{X}}_3^{k+1,p+1} \right)_{i,j} + \frac{1}{\beta} (\Lambda_1^p)_{i,j}, \left( \mathbf{D}_2 \hat{\mathbf{X}}_3^{k+1,p+1} \right)_{i,j} + \frac{1}{\beta} (\Lambda_2^p)_{i,j} \right]$ , for  $1 \leq s_3, 1 \leq j \leq r_3$ , and we assign  $0 \cdot (0/0) = 0$ , as stated in [45].

After solving the two subproblems of  $\hat{\mathbf{X}}_3$  and  $\mathbf{W}$ , the Lagrangian multipliers  $\Lambda = (\Lambda_1, \Lambda_2)^T$ , can be updated in parallel as

$$\Lambda^{p+1} = \Lambda^p + \beta \left( \mathbf{B} \hat{\mathbf{X}}_3^{k+1,p+1} + \mathbf{C} \mathbf{U}^{p+1} \right) \quad (40)$$

### 3.2.2 Update $\mathbf{A}_n$ with fixing others

The  $\mathbf{A}_n$ -sub-problem, which can be written as follows

$$\begin{aligned} \mathbf{A}_n^{k+1} &= \underset{\mathbf{A}_n}{\text{argmin}} \sum_{n=1}^N \left( \frac{\alpha_n}{2} \|\mathbf{Y}_{(n)} - \mathbf{A}_n \mathbf{X}_n\|_{\mathbf{F}}^2 + \lambda_n \|\mathbf{A}_n\|_* + \frac{\rho_n}{2} \|\mathbf{A}_n - \mathbf{A}_n^k\|_{\mathbf{F}}^2 \right), \\ \text{s.t., } \mathcal{P}_\Omega(\mathcal{Y}) &= \mathcal{F} \end{aligned} \quad (41)$$

By introducing an auxiliary variable. (41) can be rewritten as

$$\begin{aligned} \min \sum_{n=1}^N & \left( \frac{\alpha_n}{2} \|\mathbf{Y}_{(n)} - \mathbf{A}_n \mathbf{X}_n\|_F^2 + \lambda_n \|\mathbf{J}_n\|_* + \frac{\rho_n}{2} \|\mathbf{A}_n - \mathbf{A}_n^k\|_F^2 \right) \\ \text{s.t.}, & \mathbf{A}_n = \mathbf{J}_n, \mathcal{P}_\Omega(\mathcal{Y}) = \mathcal{F} \end{aligned} \quad (42)$$

The problem (42) can also be efficiently solved by the ALM method, which minimizes the following augmented Lagrangian function

$$\begin{aligned} L(\mathbf{A}_n, \mathbf{J}_n, \Gamma_n^{\mathbf{A}}) = \min \sum_{n=1}^N & \left( \frac{\alpha_n}{2} \|\mathbf{Y}_{(n)} - \mathbf{A}_n \mathbf{X}_n\|_F^2 + \lambda_n \|\mathbf{J}_n\|_* + \frac{\rho_n}{2} \|\mathbf{A}_n - \mathbf{A}_n^k\|_F^2 \right. \\ & \left. + \langle \Gamma_n^{\mathbf{A}}, \mathbf{A}_n - \mathbf{J}_n \rangle + \frac{\rho_n}{2} \|\mathbf{A}_n - \mathbf{J}_n\|_F^2 \right), \text{s.t.}, \mathcal{P}_\Omega(\mathcal{Y}) = \mathcal{F} \end{aligned} \quad (43)$$

Firstly, with others fixed, the minimization subproblem for  $\mathbf{J}_n$  can be deduced from (43) as following

$$\mathbf{J}_n^{k+1} = \operatorname{argmin}_{\mathbf{J}_n} \lambda_n \|\mathbf{J}_n\|_* + \frac{\rho_n}{2} \|\mathbf{A}_n^k - \mathbf{J}_n + \Gamma_n^{\mathbf{A}}/\rho_n\|_F^2 \quad (44)$$

The solution of variable  $\mathbf{J}_n$  can also be obtained by Lemma 1,

$$\mathbf{J}_n^{k+1} = \operatorname{SH}_{\frac{\lambda_n}{\rho_n}}(\mathbf{A}_n^k + \Gamma_n^{\mathbf{A}}/\rho_n), n = 1, 2, 3, 4, \dots, N \quad (45)$$

Secondly, with others fixed, the minimization subproblem for  $\mathbf{A}_n$  can be deduced from (43) as following

$$\begin{aligned} \mathbf{A}_n^{k+1} = \operatorname{argmin} \sum_{n=1}^N & \left( \frac{\alpha_n}{2} \|\mathbf{Y}_{(n)} - \mathbf{A}_n \mathbf{X}_n\|_F^2 \right. \\ & \left. + \rho_n \left\| \mathbf{A}_n - \frac{\mathbf{J}_n^{k+1} - \Gamma_n^{\mathbf{A}}/\rho_n + \mathbf{A}_n^k}{2} \right\|_F^2 \right) \end{aligned} \quad (46)$$

The minimization subproblem (46) of  $\mathbf{A}_n^{k+1}$  is also a convex function, which has the following closed-form solution

$$\begin{aligned} \mathbf{A}_n^{k+1} = & \left( \mathbf{X}_{(n)}^k (\mathbf{X}_n^{k+1})^T + 2\rho_n \left( \frac{\mathbf{J}_n^{k+1} - \Gamma_n^{\mathbf{A}}/\rho_n + \mathbf{A}_n^k}{2} \right) \right) \\ & \left( \mathbf{X}_n^{k+1} (\mathbf{X}_n^{k+1})^T + 2\rho_n \mathbf{I}_n \right)^\dagger, n = 1, 2, 3, 4, \dots, N \end{aligned} \quad (47)$$

Finally, based on the ADMM algorithm, the multipliers are updated by the following equations:

$$\Gamma_n^{\mathbf{A}} = \Gamma_n^{\mathbf{A}} + \mathbf{A}_n - \mathbf{J}_n \quad (48)$$

---

**Algorithm 1** :Algorithm for the proposed model-1.

---

**Require:** The observed tensor  $\mathcal{F}$ ; The set of index of observed entries; The given  $n$ -rank,  $r = (r_1, r_2, r_3)$ ; stopping criterion  $\varepsilon$ .

**Ensure:** The completed tensor.

- 1: Initialize:  $\mathbf{X}_n = \mathbf{Z}_n = 0, \mathbf{A}_n = \mathbf{J}_n = 0, \Gamma_n^{\mathbf{X}} = 0, \Gamma_n^{\mathbf{A}} = 0, n = 1, 2, 3, 4, \dots, N; \mu_{\max} = 10^6, \rho = 1.5$ , and  $k = p = 0$ .
  - 2: Repeat until convergence:
  - 3: Update  $\mathbf{X}, \mathbf{Z}, \mathbf{A}, \mathbf{J}, \mathcal{Y}, \Gamma^{\mathbf{X}}, \Gamma^{\mathbf{A}}$  via
    - 1th step: Update  $\mathbf{Z}_n$  via (24)
    - 2th step: Update  $\mathbf{X}_n, n = 1, 2, 3, 4, \dots, N$ , via (27)
    - 3th step: Update  $\mathbf{A}_n$  via (47)
    - 4th step: Update  $\mathbf{J}_n$  via (45)
    - 5th step: Update  $\mathcal{Y}$  via (50)
    - 6th step: Update the parameter via (25), (48)
  - 4: Check the convergence condition.
- 

### 3.2.3 Update $\mathcal{Y}$ with fixing others

With others fixed, the minimization subproblem for  $\mathbf{Y}_{(n)}$  can be deduced from (18) as following

$$\mathbf{Y}_{(n)}^{k+1} = \min \sum_{n=1}^N \left( \frac{\alpha_n}{2} \|\mathbf{Y}_{(n)} - \mathbf{A}_n \mathbf{X}_n\|_{\text{F}}^2 + \frac{\rho}{2} \|\mathcal{Y} - \mathcal{Y}^k\|_{\text{F}}^2 \right) \quad s.t., \mathcal{P}_{\Omega}(\mathcal{Y}) = \mathcal{F} \quad (49)$$

Then, the update of  $\mathcal{Y}_{k+1}$  can be written explicitly as

$$\mathcal{Y}^{k+1} = P_{\Omega^c} \left( \sum_{n=1}^N \alpha_n \text{fold}_n \left( \frac{\mathbf{A}_n^{k+1} \mathbf{X}_n^{k+1} + \rho_n \mathbf{Y}_{(n)}^k}{1 + \rho_n} \right) \right) + \mathcal{F} \quad (50)$$

where  $\mathcal{F}$  is the observed data,  $P_{\Omega}$  is an operator defined in subsection 2.3. The aboveproposed algorithm is applicable to the proposed model-1 and model-2, due to all variables of model-1 and model-2 are updated in the same way except  $\mathbf{X}$ . Specifically, Model-2 has one more regularizer applied to  $\mathbf{X}_3$  than Model-1. Therefore, Model-1 updates  $\mathbf{X}_n, n = 1, 2, 3, 4, \dots, N$  according to (27); Model-2 updates  $\mathbf{X}_n, n = 1, 2, 4, \dots, N$ , according to (27), while updates  $\mathbf{X}_3$  according to (36), (39) and (40).

## 3.3 Complexity and Converge Analysis

The proposed algorithm for the proposed model-1 and model-2 can then be summarized as Algorithm 1 and 2. Further, we discuss the complexity and convergence of the proposed models.

---

**Algorithm 2** :Algorithm for the proposed model-2.

---

**Require:** The observed tensor  $\mathcal{F}$ ; The set of index of observed entries; The given  $n$ -rank,  $r = (r_1, r_2, r_3)$ ; stopping criterion  $\varepsilon$ .

**Ensure:** Output: The completed tensor;

- 1: **Initialize:**  $\mathbf{A}_n^0 = \text{rand}(I_n \times r_n)$ ,  $\mathbf{X}_n^0 = \text{rand}(r_n \times \prod_{m=1, m \neq n}^N I_m)$ , ( $n = 1, 2, \dots, N$ ),  $\mathcal{Y} = \mathcal{P}_\Omega(\mathcal{F})$ .
  - 2: **repeat**
    - 1th step: Update  $\mathbf{Z}_n$  via (24)
    - 2th step: Update  $\mathbf{X}_n, n = 1, 2, 4, \dots, N$ , via (27)
    - 3th step: Update  $\mathbf{X}_3$  via
  - 3: **repeat**
    - 3-1th step: Update  $\mathbf{X}_3$  via (36)
    - 3-2th step: Update  $\mathbf{U}$  via (39)
    - 3-3th step: Update  $\Lambda$  via (40)
  - 4: **until** converged
    - 4th step: Update  $\mathbf{J}_n$  via (45)
    - 5th step: Update  $\mathbf{A}_n$  via (47)
    - 6th step: Update  $\mathcal{Y}$  via (50)
    - 7th step: Update the parameter via (25), (48)
  - 5: **until** converged
- 

### 3.3.1 Complexity Analysis

The cost of computing  $\mathbf{X}_n$  is  $O(I_n r_n^2 + I_n r_n s_n + r_n^2 s_n)$ , calculating  $\mathbf{Z}_n$  has a complexity of  $O(\Pi_{j \neq n} I_j \times r_n^2)$ , the complexity of updating  $\mathbf{J}_n$  is  $O(I_n r_n^2)$ , calculating  $\mathbf{A}_n$  has a complexity of  $O(I_n r_n^2 + I_n r_n s_n + r_n^2 s_n)$  and calculating  $[\mathbf{W}_1, \mathbf{W}_2]$  has a complexity of  $O(s_3 r_3)$ , the complexity of updating  $\text{vec}(\hat{\mathbf{X}}_3)$  is  $O(2s_3 r_3^2 + s_3 r_3 \log s_3)$ , calculating  $\mathcal{Y}$  has a complexity of

$$O(r_1 I_1 s_1 + \dots + r_N I_N s_N).$$

Therefore, the total complexity of the proposed algorithm can be obtained by counting the complexity of the above variables. For easy viewing, we list the total complexity of the proposed model-1 and model-2 in (51) and (52) respectively.

$$O\left(\sum_n (3I_n r_n^2 + \Pi_{j \neq n} I_j \times r_n^2 + 3I_n r_n s_n + 2r_n^2 s_n)\right) \quad (51)$$

$$\begin{aligned} &O\left(\sum_{n \neq 3} (3I_n r_n^2 + \Pi_{j \neq n} I_j \times r_n^2 + 3I_n r_n s_n + 2r_n^2 s_n)\right) \\ &+ I_3 r_3^2 + 2l_3 r_3 s_3 + 3r_3^2 s_3 + r_3 s_3 \log s_3 \end{aligned} \quad (52)$$

### 3.3.2 Convergence Analysis

In this section, the convergence of the proposed models are proved theoretically by using the block successive upper-bound minimization (BSUM)[46]. The BSUM is an alternative inexact block coordinate descent method be proposed recently, which is designed for non-smooth optimization problem.

**Lemma 1** [46, 45]. Given the problem  $\min f(x)$  s.t.  $x \in \mathcal{X}$ , where  $\mathcal{X}$  is the feasible set. Assume  $h(x, x^{k-1})$  is an approximation of  $f(x)$  at the  $(k-1)$ -th iteration, which satisfied the following conditions:

- 1)  $h_i(y_i, y) = f(y), \forall y \in \mathcal{X}, \forall i;$
- 2)  $h_i(x_i, y) \geq f(y_1, \dots, y_{i-1}, x_i, y_{i+1}, \dots, y_n), \forall x_i \in \mathcal{X}_i, \forall y \in \mathcal{X}, \forall i;$
- 3)  $h'_i(x_i, y; d_i)|_{x_i=y_i} = f'(y; d), v_i = (0, \dots, d_i \dots 0)$  s.t.  $y_i + d_i \in \mathcal{X}_i, \forall i;$
- 4)  $h_i(x_i, y)$  is continuous in  $(x_i, y), \forall i;$

(53)

where  $h_i(x_i, y)$  is the sub-problem with respect to the  $i$ -th block and  $f'(y; d)$  is the direction derivative of  $f$  at the point  $y$  in direction  $d$ . Suppose  $h_i(x_i, y)$  is quasi-convex in  $x_i$  for  $i = 1, \dots, n$ . Furthermore, assume that each sub-problem  $\arg\min h_i(x_i, x^{k-1})$ , s.t.  $x \in \mathcal{X}_i$  has a unique solution for any point  $x^{k-1} \in \mathcal{X}$ . Then, the iterates generated by the BSUM algorithm converge to the set of coordinatewise minimum of  $f$ .

**Theorem 1.** The iterates generated by (16) converge to the set of coordinatewise minimizers.

**Proof.** It is easy to verify that  $g(\mathcal{S}, \mathcal{S}^k)$  is an approximation and a global upper bound of  $f(\mathcal{S})$  at the  $k$ -th iteration, which satisfies the following conditions:

- 1)  $g_i(\mathcal{S}_i, \mathcal{S}) = f(\mathcal{S}), \forall \mathcal{S}, i = 1, 2, 3,$
- 2)  $g_i(\bar{\mathcal{S}}_i, \mathcal{S}) \geq f(\mathcal{S}_1, \dots, \bar{\mathcal{S}}_i, \dots, \mathcal{S}_3), \forall \bar{\mathcal{S}}_i, \forall \mathcal{S}, i = 1, 2, 3$
- 3)  $g'_i(\bar{\mathcal{S}}_i, \mathcal{S}; \mathbf{M}_i)|_{\bar{\mathcal{S}}_i=\mathcal{S}_i} = f'(\mathcal{S}; \mathbf{M}^i), \forall \mathbf{M}^i = (0, \dots, \mathbf{M}_i, \dots, 0),$
- 4)  $g_i(\bar{\mathcal{S}}_i, \mathcal{S})$  is continuous in  $(\bar{\mathcal{S}}_i, \mathcal{S}), i = 1, 2, 3,$

(54)

where  $\mathcal{S} = (\mathbf{X}, \mathbf{A}, \mathcal{Y})$ , and  $\mathcal{S}_i$  equal  $\mathbf{X}, \mathbf{A}, \mathcal{Y}$  for  $i = 1, 2, 3$ , respectively. In addition, the sub-problem  $g_i(i = 1, 2, 3)$  is strictly convex with respect to  $\mathbf{X}, \mathbf{A}$  and  $\mathcal{Y}$  respectively and each sub-problem of  $g_i$  has a unique solution. Therefore, all assumptions in **Lemma 1** are satisfied. According to the conclusion of **Lemma 1**, the **Theorem 1** is valid, and the proposed algorithm is theoretically convergent.

## 4 Numerical experiments

In order to verify the effectiveness of the proposed model-1 and model-2, we carry out lots of experiments on three types of public tensor data sets, i.e., video data, MRI data and hyperspectral image data, which have been frequently used to interpret the tensor completion performance of different models. Four different



completion models are selected as comparison methods, i.e., TMac [41], TV based method MF-TV [45], single nuclear norm based method TNN [28] and PSTNN based on partial sum of tubal nuclear norm [40].

To accurately evaluate the performance of the models, we mainly use two types of standards for evaluation. The first is the visual evaluation of the restored data, which is a qualitative evaluation standard. The second is the five quantitative picture quality indices (PQIs), including the peak signal-to-noise ratio (PSNR) [51], structural similarity index (SSIM) [52], feature similarity (FSIM) [53], erreur relative globale adimensionnelle de synthèse (ERGAS) [54], the mean the spectral angle mapper (SAM) [55]. Larger PSNR, SSIM, FSIM and and smaller ERGAS, SAM indicate the better the restoration performance of the corresponding model is. Since the experimental datasets are all third-order tensors, the PQIs for each frontal slice in the restored tensor are first calculated, and then the mean of these PQIs are finally used to evaluate the performance of the models. All experiments were performed on MATLAB 2018b, the CPU of the computer is Inter core i7@2.2GHz and the memory is 64GB.

For an tensor  $\mathcal{Y} \in \mathbb{R}^{I_1 \times \dots \times I_N}$ , let  $S_{\text{number}}$  denotes the number of sampled entries in its index set  $\Omega$ . Then the sampling ratio (SR) can be defined as:

$$\text{SR} = \frac{S_{\text{number}}}{\prod_{n=1}^N I_n}. \quad (55)$$

where the sampled entries are chosen randomly from a tensor  $\mathcal{Y}$  by a uniform distribution. In the proposed algorithm for model-1 and model-2, the inputs include the observed tensor  $\mathcal{F} \in \mathbb{R}^{I_1 \times I_2 \times I_3}$ , the stopping criteria  $\epsilon$ , the regularized parameters  $\alpha, \beta, \lambda, \tau$ , and the penalty parameter  $\beta$ . All parameters are empirically, specifically, the stopping criterion  $\epsilon$  and the weights  $\alpha_i = 1/3 (i = 1, 2, 3)$  of the proposed model-1 and model-2 are set to be  $10^{-5}$  and  $1/3$  for all experiments; the regularization parameter  $\mu$  and the penalty parameter  $\beta$  for model-2 are set as 0.5 and 10, respectively; finally, the proximal parameter  $\rho$  and regularized parameters  $\lambda, \tau$  are all set as 0.1 for all experiments of model-1 and model-2.

## 4.1 Video

In this part, the proposed model is applied to two video datasets to verify the performance of the model, i.e., video dataset "suzie" and "hall"<sup>1</sup>, both of which are colored using YUV format. The sizes of both video datasets are  $144 \times 176 \times 150$ . The sampling rates (SR) are set as 5%, 10% and 20%.

For Quantitative comparison, Table Table 1 and 2 lists the PQIs of all the compared models in the four sampling rates. The best results for each PQI are marked in bold. It is clear from Table 1 and 2 that in all cases our model-2 obtained the best results, and our model-1 obtained the suboptimal results compared to other methods. For visual evaluation, we show one frontal slice of the recovered results with different random sampling rates in Fig. 2, Fig. 3,

---

<sup>1</sup><http://trace.eas.asu.edu/yuv/>

Table 1: The averaged MPSNR, MSSIM, MFSIM, ERGA and MSAM of the recovered results on video "suzie" by Tmac, MF-TV, TNN, PSTNN and the proposed model-1, model-2 with different sampling Rate. The best value is highlighted in bolder fonts.

method	Dataset:		Suzie	SR = 0.05			
	Nosiy	our model-2	our model-1	MF-TV	Tmac	PSTNN	TNN
PSNR	7.259	<b>30.268</b>	26.663	13.801	23.385	17.447	22.005
SSIM	0.009	<b>0.85</b>	0.733	0.094	0.622	0.192	0.563
FSIM	0.454	<b>0.904</b>	0.852	0.42	0.792	0.59	0.776
ERGA	1057.282	<b>76.304</b>	115.628	501.117	167.927	327.678	194.844
MSAM	77.324	<b>3.258</b>	4.775	24.095	6.927	13.775	7.797
SR = 0.1							
method	Nosiy	our model-2	our model-1	MF-TV	Tmac	PSTNN	TNN
PSNR	7.493	<b>32.272</b>	30.002	22.356	26.189	26.647	26.032
SSIM	0.014	<b>0.887</b>	0.832	0.605	0.74	0.68	0.692
FSIM	0.426	<b>0.928</b>	0.899	0.758	0.838	0.843	0.846
ERGA	1029.096	<b>60.723</b>	79.383	196.059	124.369	117.104	124.923
MSAM	71.725	<b>2.678</b>	3.385	6.99	5.423	5.171	5.405
SR = 0.2							
method	Nosiy	our model-2	our model-1	MF-TV	Tmac	PSTNN	TNN
PSNR	8.005	<b>34.492</b>	33.745	32.064	27.274	30.566	30.561
SSIM	0.02	<b>0.921</b>	0.909	0.872	0.782	0.829	0.831
FSIM	0.391	<b>0.95</b>	0.943	0.916	0.853	0.91	0.911
ERGA	970.285	<b>46.89</b>	51.759	66.692	109.627	75.472	75.598
MSAM	63.522	<b>2.142</b>	2.329	2.81	4.812	3.399	3.395

Fig. 4, Fig. 5 and Fig. 6. Compared to other models, it can be seen that the result of our models is closest to the original reference image, especially at low sampling rates. Specifically, as shown in Fig. 6, Fig. 2 and Fig. 3, when the sampling rate is 0.05 and 0.1, the advantages of the proposed model are most obvious. The proposed model restores most of the structural information of the image, while the image restored by the competitive method contains only the outline of the image. At a higher sampling rate, as shown in Fig. 4 and Fig. 6, the proposed model and competitive method both recover the main structural information of the image, but the proposed method recovers more texture and detail information.

## 4.2 MRI

In this part, to further verify the versatility of our model for different datasets, the proposed model is applied to MRI dataset, i.e., the cubical MRI data <sup>2</sup>. The sizes of the dataset is  $150 \times 150 \times 181$ . The sampling rates (SR) are set as 5%, 10%, 20% and 30%.

Table 3 summarizes the PQIs of the recovered results at the four sampling

<sup>2</sup>[http://brainweb.bic.mni.mcgill.ca/brainweb/selection\\_normal.html](http://brainweb.bic.mni.mcgill.ca/brainweb/selection_normal.html)

Table 2: The averaged MPSNR, MSSIM, MFSIM, ERGA and MSAM of the recovered results on video "hall" by Tmac, MF-TV, TNN, PSTNN and the proposed model-1, model-2 with different sampling Rate. The best value is highlighted in bolder fonts.

method	Dataset:		Hall	SR =0.05			
	Nosiy	our model-2	our model-1	MF-TV	Tmac	PSTNN	TNN
PSNR	4.82	<b>29.571</b>	26.647	13.539	22.101	16.075	20.78
SSIM	0.007	<b>0.915</b>	0.862	0.412	0.675	0.36	0.636
FSIM	0.387	<b>0.935</b>	0.899	0.612	0.789	0.672	0.792
ERGA	1225.779	<b>73.007</b>	100.944	452.351	168.866	335.52	195.315
MSAM	77.299	<b>2.193</b>	2.727	12.865	3.818	8.64	4.299
SR = 0.1							
method	Nosiy	our model-2	our model-1	MF-TV	Tmac	PSTNN	TNN
PSNR	5.055	<b>32.103</b>	30.241	24.855	26.936	29.014	28.433
SSIM	0.013	<b>0.936</b>	0.918	0.829	0.854	0.892	0.905
FSIM	0.393	<b>0.953</b>	0.939	0.873	0.888	0.934	0.936
ERGA	1193.075	<b>55.089</b>	67.967	131.422	97.185	77.395	82.259
MSAM	71.7	<b>1.824</b>	2.11	3.669	2.404	2.417	2.46
SR = 0.2							
method	Nosiy	our model-2	our model-1	MF-TV	Tmac	PSTNN	TNN
PSNR	5.567	<b>34.045</b>	33.647	33.006	27.648	33.629	33.691
SSIM	0.025	<b>0.953</b>	0.952	0.94	0.869	0.961	0.962
FSIM	0.403	<b>0.965</b>	0.964	0.954	0.897	0.973	0.974
ERGA	1124.737	<b>43.939</b>	46.002	50.971	89.271	46.123	45.851
MSAM	63.507	<b>1.546</b>	1.584	1.779	2.226	1.584	1.565

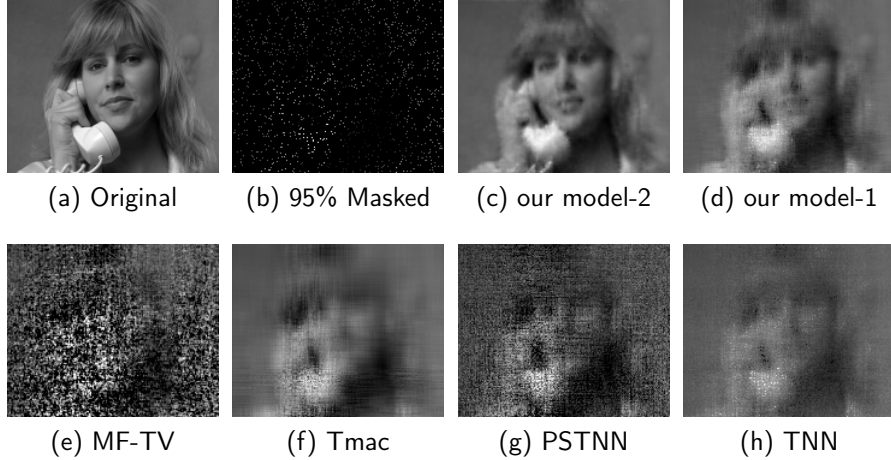


Figure 2: The image of the recovered video for “suzie” by our model 1 and 2, MF-TV, Tmac, PSTNN and TNN. The sampling rates (SR) is 5%.

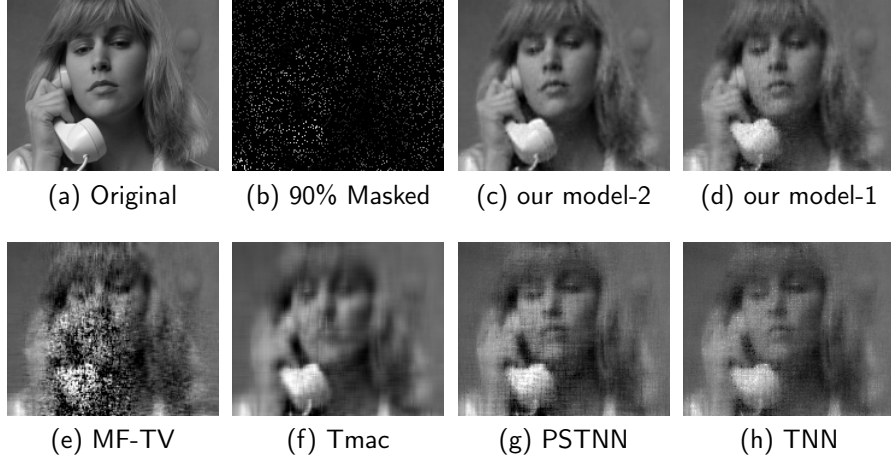


Figure 3: The image of the recovered video for “suzie” by our model 1 and 2, MF-TV, Tmac, PSTNN and TNN. The sampling rates (SR) is 10%.

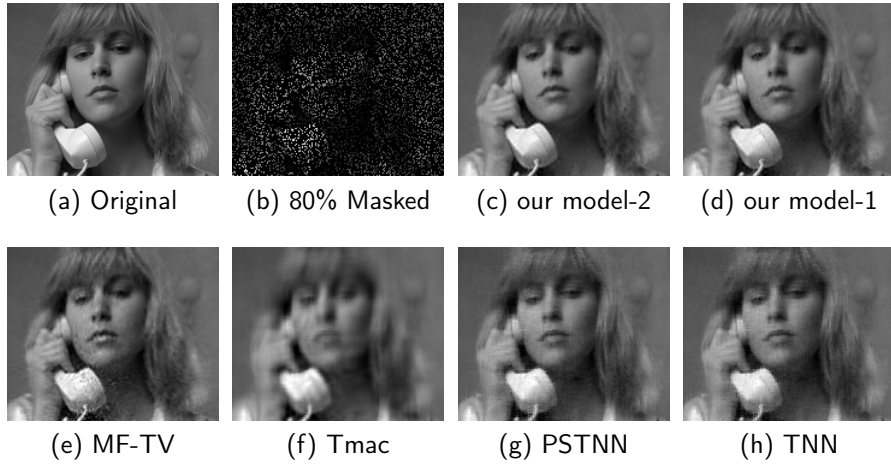


Figure 4: The image of the recovered video for “suzie” by our model-1 and model-2, MF-TV, Tmac, PSTNN and TNN. The sampling rates (SR) is 20%.

rates in the MRI dataset. It can be clearly found that our proposed model achieves higher PQIs than the comparative model. And the same advantage of our model can also be seen in Fig. 12, which illustrates the PSNR, SSIM and FSIM values slice by slice in all sampling rates. For visual comparison, at a sampling rate of 0.1, Fig. 8, Fig. 9, Fig. 10 and Fig. 11 show the grayscale images of the original MRI data, the sampled data, and the different recovery results. It can be seen that our model can better retain the local details and

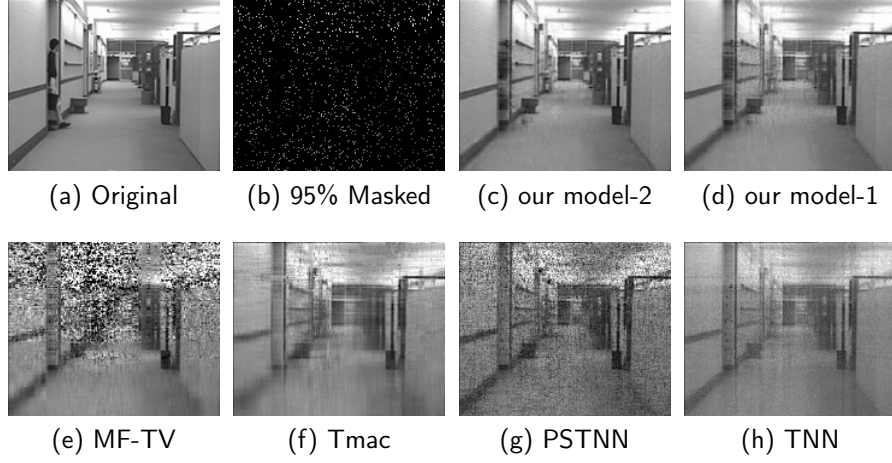


Figure 5: The image of the recovered video for “hall” by our model-1 and model-2, MF-TV, Tmac, PSTNN and TNN. The sampling rates (SR) is 5%.

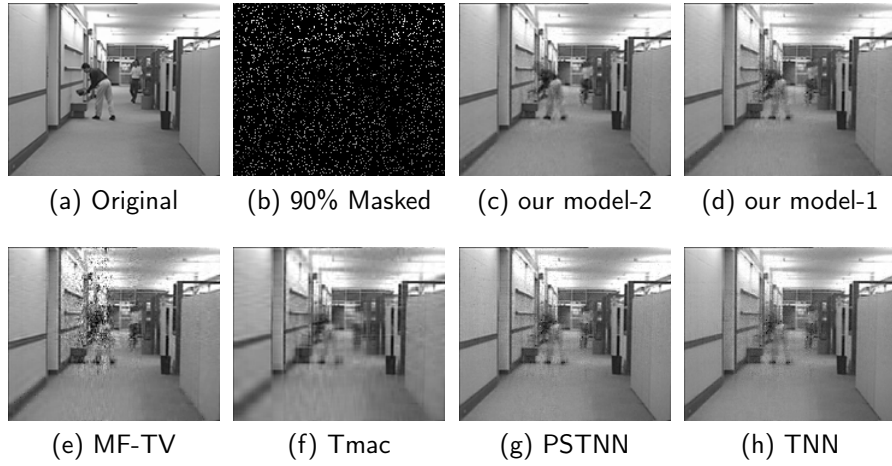


Figure 6: The image of the recovered video “hall” by our model-1 and model-2, MF-TV, Tmac, PSTNN and TNN. The sampling rates (SR) is 10%.

texture information of the image, and effectively restore the main structure of the image. Therefore, one can see that the recovered data obtained by our models has the best visual evaluation.

Table 3: The averaged MPSNR, MSSIM, MFSIM, ERGA and MSAM of the recovered results on MRI by Tmac, MF-TV, TNN, PSTNN and the proposed model-1, model-2 with different sampling Rate. The best value is highlighted in bolder fonts.

method	Nosiy	Dataset:	MRI	SR =0.05			
		our model-2	our model-1	MF-TV	Tmac	PSTNN	TNN
PSNR	10.258	<b>24.048</b>	23.54	12.332	20.51	15.859	18.218
SSIM	0.228	<b>0.696</b>	0.597	0.099	0.45	0.224	0.27
FSIM	0.473	<b>0.817</b>	0.791	0.52	0.711	0.642	0.646
ERGA	1030.203	<b>212.967</b>	230.079	814.747	339.385	545.77	434.774
MSAM	76.54	<b>20.912</b>	22.626	55.603	31.367	36.355	31.11
SR = 0.1							
method	Nosiy	our model-2	our model-1	MF-TV	Tmac	PSTNN	TNN
PSNR	10.492	<b>31.9</b>	28.085	15.406	21.411	22.061	22.535
SSIM	0.241	<b>0.919</b>	0.798	0.25	0.531	0.482	0.536
FSIM	0.511	<b>0.932</b>	0.879	0.587	0.732	0.764	0.78
ERGA	1002.8	<b>86.415</b>	134.58	584.827	308.655	275.473	266.753
MSAM	70.986	<b>14.285</b>	18.022	41.826	29.345	24.585	24.6
SR = 0.2							
method	Nosiy	our model-2	our model-1	MF-TV	Tmac	PSTNN	TNN
PSNR	11.003	<b>35.842</b>	34.166	27.062	22.33	29.152	28.571
SSIM	0.271	<b>0.963</b>	0.941	0.737	0.586	0.804	0.802
FSIM	0.564	<b>0.965</b>	0.954	0.84	0.754	0.895	0.891
ERGA	945.583	<b>54.522</b>	66.369	173.636	276.269	127.133	136.182
MSAM	62.887	<b>11.855</b>	13.38	21.792	27.267	17.513	17.855
SR = 0.3							
method	Nosiy	our model-2	our model-1	MF-TV	Tmac	PSTNN	TNN
PSNR	11.582	<b>37.991</b>	37.301	36.355	23.077	32.608	32.481
SSIM	0.303	<b>0.977</b>	0.971	0.954	0.625	0.895	0.89
FSIM	0.597	<b>0.978</b>	0.975	0.962	0.773	0.939	0.939
ERGA	884.608	<b>42.534</b>	46.165	52.449	252.057	85.845	87.312
MSAM	56.216	<b>10.284</b>	11.019	13.849	25.722	14.858	14.879

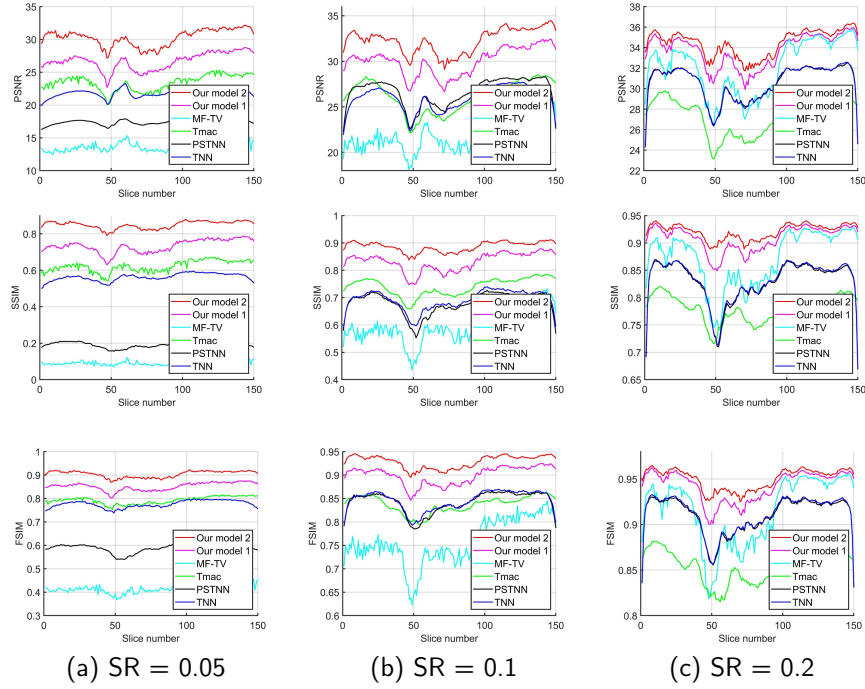


Figure 7: The PSNR, SSIM and FSIM of the recovered video "suzie" by MF-TV, Tmac, TNN, PSTNN and our model-1 and model-2 for all bands, respectively.

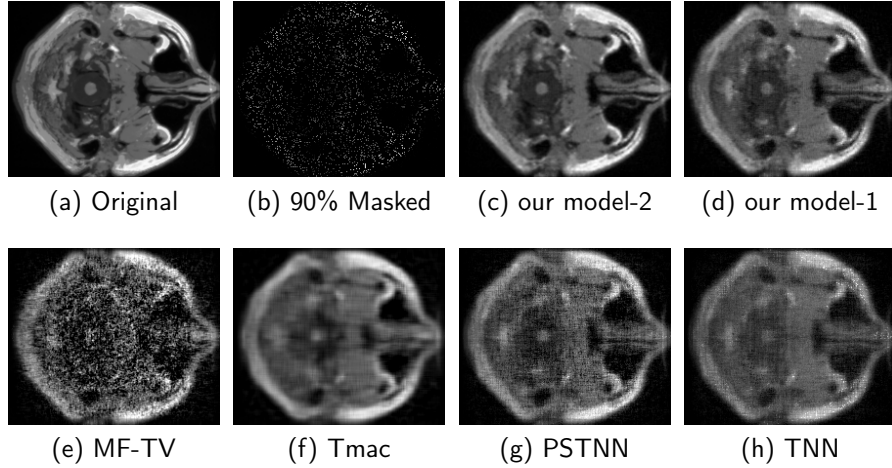


Figure 8: The image of the recovered MRI by our model-1 and model-2, MF-TV, Tmac, PSTNN and TNN. The sampling rates (SR) is 10%.

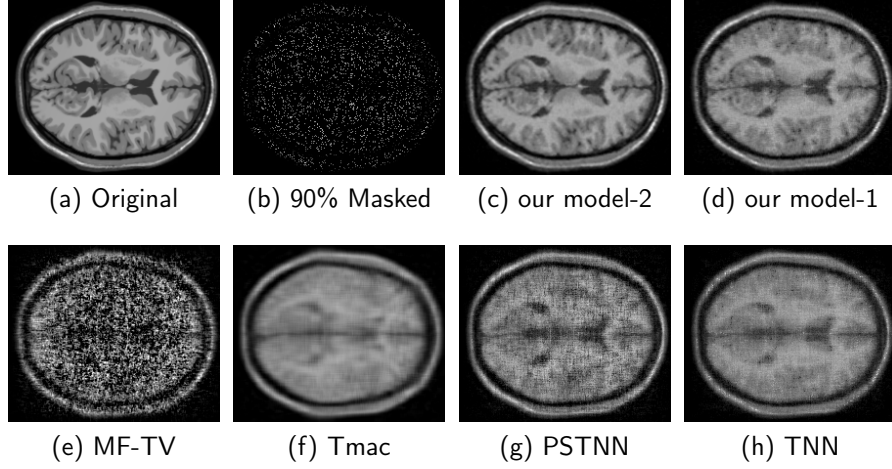


Figure 9: The image of the recovered MRI by our model-1 and model-2, MF-TV, Tmac, PSTNN and TNN. The sampling rates (SR) is 10%.

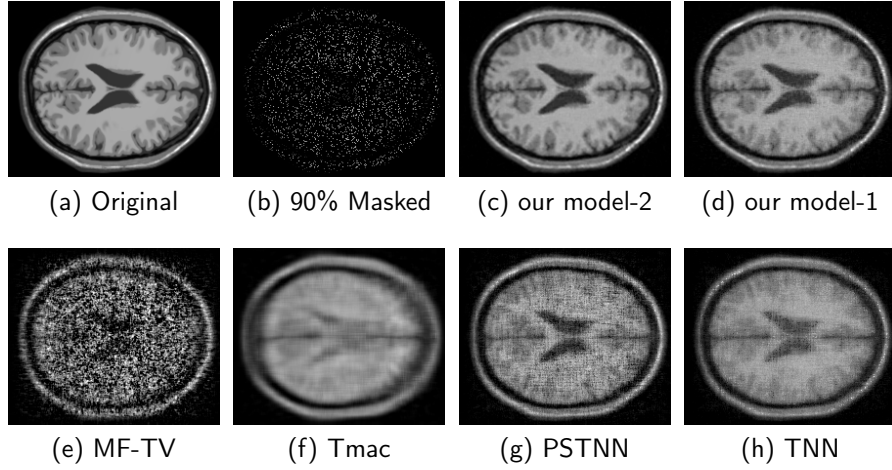


Figure 10: The image of the recovered MRI by our model 1 and 2, MF-TV, Tmac, PSTNN and TNN. The sampling rates (SR) is 10%.

### 4.3 Hyperspectral image

In this subsection, we select two HSI data to apply simulated experiments. The first dataset is the Pavia City<sup>3</sup> which was filmed by the reflection optical system imaging spectrometer (ROSIS-03). The size of Pavia Centre is  $1096 \times 1096$ , with

<sup>3</sup>[http://www.ehu.es/ccwintco/index.php/Hyperspectral\\_Remote\\_Sensing\\_Scenes](http://www.ehu.es/ccwintco/index.php/Hyperspectral_Remote_Sensing_Scenes)



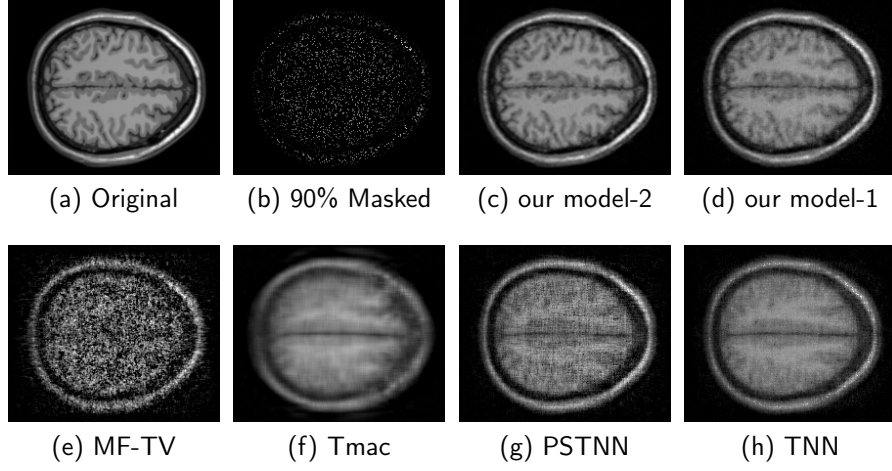


Figure 11: The image of the recovered MRI by our model-1 and model-2, MF-TV, Tmac, PSTNN and TNN. The sampling rates (SR) is 10%.

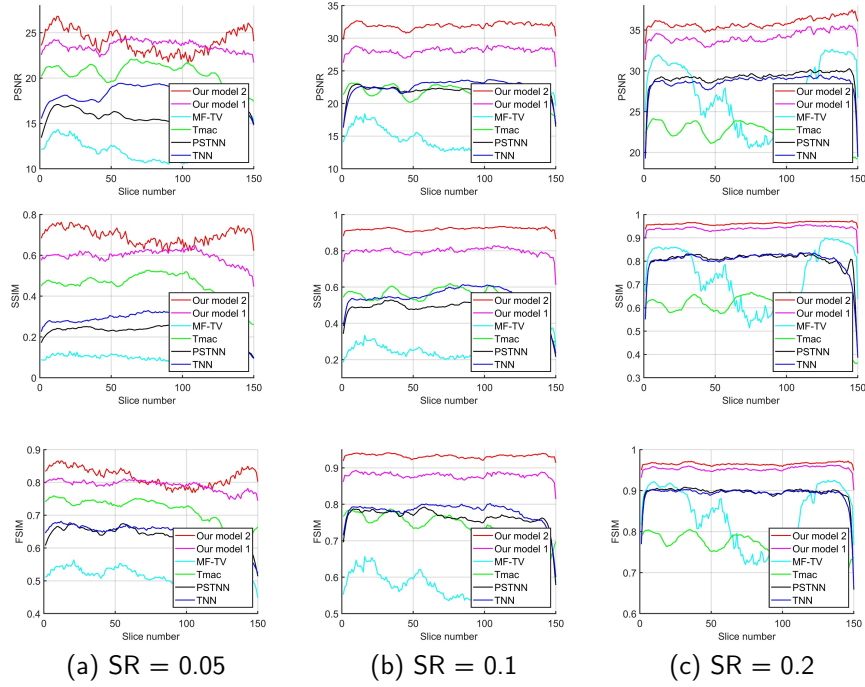


Figure 12: The PSNR, SSIM and FSIM of the recovered MRI by MF-TV, Tmac, TNN, PSTNN and our model-1 and model-2 for all bands, respectively.

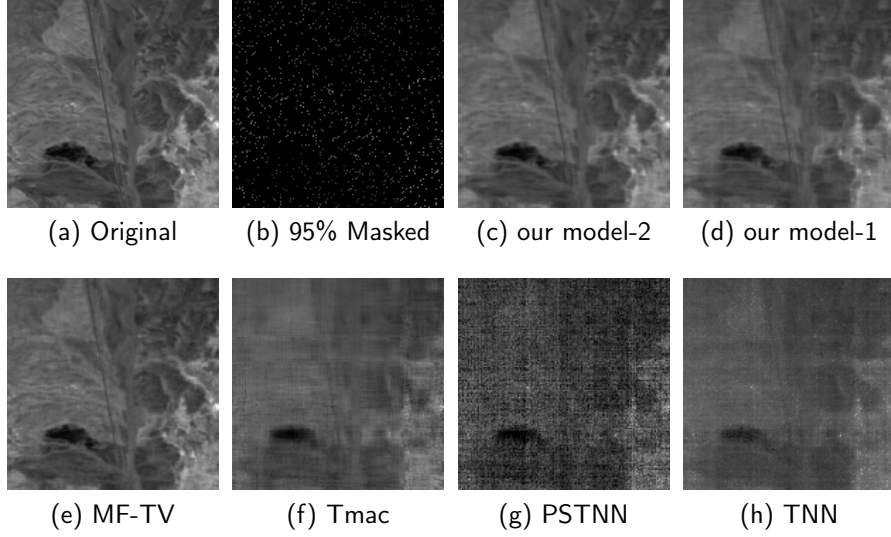


Figure 13: The image of the recovered HSI "Cuprite" by our model-1 and model-2, MF-TV, Tmac, PSTNN and TNN. The sampling rates (SR) is 5%.

a total of 102 bands. Because some of the bands in the Pavia City Centre dataset are heavily polluted by noise, they can not be used as a reference for restoration results. Therefore, this part of the heavily polluted data has been removed. Due to space limitations, we select data with a spatial size of  $200 \times 200$  and a total of 80 bands for simulated experiments in this part. The second dataset is the Airborne Visible/Infrared Imaging Spectrometer (AVIRIS) Cuprite data<sup>4</sup>. The size of it is  $150 \times 150 \times 210$ . The sampling rate is set to 0.025, 0.05 and 0.1.

Table 4 and Table 5 list the PQIs of the results restored by the proposed model and the competition model at three sampling rates. Fig. 14 lists the PSNR, SSIM and FSIM of each frontal slice of the recovered "Cuprite" for all methods at sampling rates of 0.025 and 0.05. Fig. 13 shows the recovered "Cuprite" for all methods at sampling rate of 0.05. Fig. 17 lists the PSNR, SSIM and FSIM of each frontal slice of the recovered "Pavia" for all methods at sampling rates of 0.025, 0.05 and 0.1. Fig. 15 and Fig. 16 shows the recovered "Pavia" for all methods at sampling rates of 0.025 and 0.05. It can be clearly seen that the two proposed methods not only obtain the highest PQIs, but also recover the architectural information of the image, and restore more spatial details than comparison methods, especially at low sampling rates. Therefore, one can see that the recovered data obtained by our models has the best visual evaluation and PQIs.

<sup>4</sup><http://aviris.jpl.nasa.gov/html/aviris.freedata.html>

Table 4: The averaged MPSNR, MSSIM, MFSIM, ERGA and MSAM of the recovered results on hyperspectral image "Cuprite" by Tmac, MF-TV, TNN, PSTNN and the proposed model-1, model-2 with different sampling Rate. The best value is highlighted in bolder fonts.

method	Dataset:		HSI	SR =0.025			
	Nosiy	our model-2	our model-1	MF-TV	Tmac	PSTNN	TNN
PSNR	7.666	<b>34.983</b>	31.985	26.115	21.25	13.387	22.783
SSIM	0.007	<b>0.877</b>	0.807	0.539	0.412	0.124	0.554
FSIM	0.48	<b>0.91</b>	0.861	0.765	0.755	0.613	0.775
ERGA	1043.633	<b>47.3</b>	64.636	237.074	235.594	539.574	245.333
MSAM	81.221	<b>1.483</b>	1.833	12.913	7.842	17.98	9.156
SR = 0.05							
method	Nosiy	our model-2	our model-1	MF-TV	Tmac	PSTNN	TNN
PSNR	7.779	<b>38.433</b>	35.402	34.684	28.945	20.621	26.579
SSIM	0.01	<b>0.936</b>	0.893	0.845	0.712	0.31	0.663
FSIM	0.471	<b>0.959</b>	0.928	0.915	0.846	0.735	0.836
ERGA	1030.139	<b>34.53</b>	45.581	89.372	93.352	234.445	154.292
MSAM	77.268	<b>1.225</b>	1.481	4.386	3.278	7.886	5.413
SR = 0.1							
method	Nosiy	our model-2	our model-1	MF-TV	Tmac	PSTNN	TNN
PSNR	8.013	<b>41.182</b>	39.084	40.888	35.627	35.51	35.015
SSIM	0.014	<b>0.961</b>	0.946	0.957	0.885	0.907	0.897
FSIM	0.451	<b>0.979</b>	0.968	0.978	0.931	0.951	0.943
ERGA	1002.75	<b>28.338</b>	33.934	34.263	44.518	54.421	57.537
MSAM	71.695	<b>1.098</b>	1.25	1.46	1.445	2.072	2.192

## 5 Conclusions

In this paper, we propose two new low-rank models based on tensor-based modal matrix decomposition for tensor completion. Instead of the traditional single nuclear norm, we adopt a kind of Schatten- $p$  quasi-norm named Double Nuclear norm to formulate the low-rank structure of the modal matrix of underlying tensor with non-linear metric, which is called model-1. Further, in order to take advantage of the local smoothing structure of the target tensor, we integrate total variation regularization with model-1 as model-2. It was demonstrated that our numerical scheme converged to the coordinatewise minimizers. The proposed model has been evaluated on three types of public data sets, which show that our algorithm can recover a variety of low-rank tensors from significantly fewer samples than the compared methods.

## References

- [1] T. Ding, M. Sznaiier, O. I. Camps, A rank minimization approach to video inpainting, in: 2007 IEEE 11th International Conference on Computer Vision, IEEE, 2007, pp. 1–8.

Table 5: The averaged MPSNR, MSSIM, MFSIM, ERGA and MSAM of the recovered results on hyperspectral image "Pavia" by Tmac, MF-TV, TNN, PSTNN and the proposed model-1, model-2 with different sampling Rate. The best value is highlighted in bolder fonts.

		Dataset:	Pavia	SR =0.025			
method	Nosiy	our model-2	our model-1	MF-TV	Tmac	PSTNN	TNN
PSNR	13.388	<b>29.353</b>	24.781	20.132	20.765	17.39	19.984
SSIM	0.014	<b>0.859</b>	0.654	0.385	0.379	0.288	0.344
FSIM	0.436	<b>0.905</b>	0.801	0.726	0.717	0.705	0.639
ERGA	787.86	<b>124.945</b>	211.791	450.292	344.451	496.92	369.941
MSAM	81.947	<b>6.612</b>	8.622	36.188	16.917	34.622	14.16
SR = 0.05							
method	Nosiy	our model-2	our model-1	MF-TV	Tmac	PSTNN	TNN
PSNR	13.5	<b>33.066</b>	28.46	25.442	24.6	21.028	22.557
SSIM	0.025	<b>0.938</b>	0.832	0.643	0.64	0.512	0.538
FSIM	0.469	<b>0.958</b>	0.893	0.835	0.798	0.791	0.752
ERGA	777.776	<b>81.615</b>	139.446	316.6	216.234	326.121	276.113
MSAM	77.699	<b>5.024</b>	7.267	26.414	10.31	22.871	13.08
SR = 0.1							
method	Nosiy	our model-2	our model-1	MF-TV	Tmac	PSTNN	TNN
PSNR	13.736	<b>37.347</b>	32.818	36.064	26.523	29.518	27.363
SSIM	0.046	<b>0.976</b>	0.932	0.938	0.737	0.857	0.806
FSIM	0.516	<b>0.985</b>	0.954	0.965	0.832	0.923	0.889
ERGA	756.907	<b>50.103</b>	85.931	93.891	172.184	132.084	163.529
MSAM	71.908	<b>3.727</b>	5.896	9.397	8.871	11.236	10.825

- [2] H. Ji, C. Liu, Z. Shen, Y. Xu, Robust video denoising using low rank matrix completion, in: 2010 IEEE Computer Society Conference on Computer Vision and Pattern Recognition, IEEE, 2010, pp. 1791–1798.
- [3] Y. Peng, A. Ganesh, J. Wright, W. Xu, Y. Ma, Rasl: Robust alignment by sparse and low-rank decomposition for linearly correlated images, IEEE transactions on pattern analysis and machine intelligence 34 (11) (2012) 2233–2246.
- [4] C. Lang, G. Liu, J. Yu, S. Yan, Saliency detection by multitask sparsity pursuit, IEEE transactions on image processing 21 (3) (2011) 1327–1338.
- [5] L. Zhuang, H. Gao, J. Huang, N. Yu, Semi-supervised classification via low rank graph, in: 2011 Sixth International Conference on Image and Graphics, IEEE, 2011, pp. 511–516.
- [6] K. A. Patwardhan, G. Sapiro, M. Bertalmio, Video inpainting under constrained camera motion, IEEE Transactions on Image Processing 16 (2) (2007) 545–553.
- [7] J. Yuan, Mri denoising via sparse tensors with reweighted regularization, Applied Mathematical Modelling 69 (2019) 552–562.

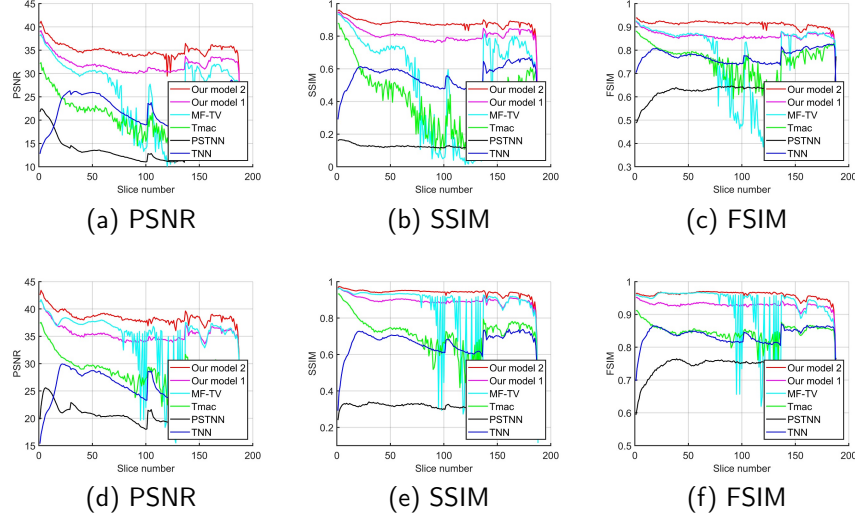


Figure 14: The PSNR, SSIM and FSIM of the recovered HSI "Cuprite" by MF-TV, Tmac, TNN, PSTNN and our model-1 and model-2 for all bands, respectively.(a)-(c): 97.5% entries missing, (d)-(f): 95% entries missing.

- [8] A. C. Sauve, A. O. Hero, W. L. Rogers, S. J. Wilderman, N. H. Clinthorne, 3d image reconstruction for a compton spect camera model, *IEEE Transactions on Nuclear Science* 46 (6) (1999) 2075–2084.
- [9] H.-J. Zeng, X.-Z. Xie, K. Wen-Feng, S. Cui, J.-F. Ning, Hyperspectral image denoising via combined non-local self-similarity and local low-rank regularization, *IEEE Access* 8 (2020) 50190–50208.
- [10] J.-T. Sun, H.-J. Zeng, H. Liu, Y. Lu, Z. Chen, Cubesvd: a novel approach to personalized web search, in: *Proceedings of the 14th international conference on World Wide Web*, 2005, pp. 382–390.
- [11] N. Kreimer, M. D. Sacchi, A tensor higher-order singular value decomposition for prestack seismic data noise reduction and interpolation, *Geophysics* 77 (3) (2012) V113–V122.
- [12] S. Ma, D. Goldfarb, L. Chen, Fixed point and bregman iterative methods for matrix rank minimization, *Mathematical Programming* 128 (1-2) (2011) 321–353.
- [13] K.-C. Toh, S. Yun, An accelerated proximal gradient algorithm for nuclear norm regularized linear least squares problems, *Pacific Journal of optimization* 6 (615-640) (2010) 15.
- [14] C. Chen, B. He, X. Yuan, Matrix completion via an alternating direction method, *IMA Journal of Numerical Analysis* 32 (1) (2012) 227–245.

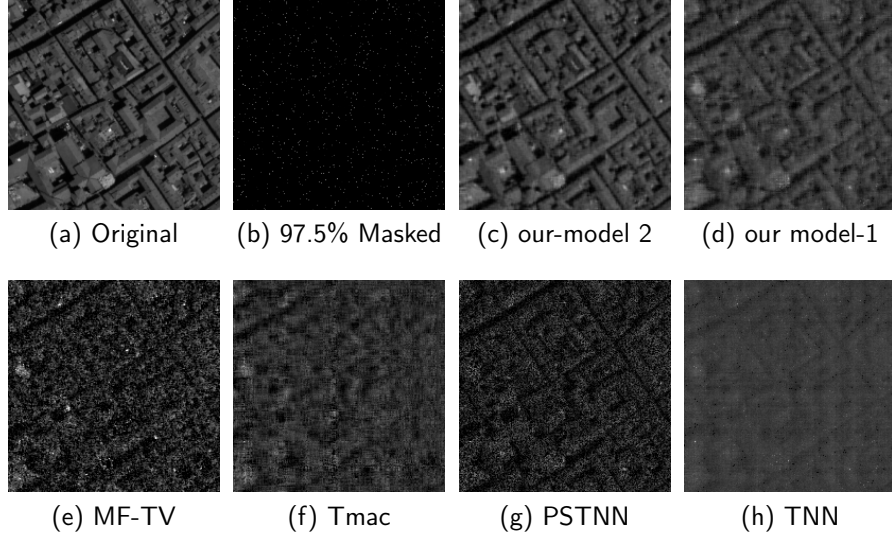


Figure 15: The image of the recovered HSI "Pavia" by our model-1 and model-2, MF-TV, Tmac, PSTNN and TNN. The sampling rates (SR) is 2.5%.

- [15] Y. Wu, H. Tan, Y. Li, F. Li, H. He, Robust tensor decomposition based on cauchy distribution and its applications, *Neurocomputing* 223 (2017) 107–117.
- [16] J. Liu, P. Musialski, P. Wonka, J. Ye, Tensor completion for estimating missing values in visual data, *IEEE transactions on pattern analysis and machine intelligence* 35 (1) (2012) 208–220.
- [17] M. Yuan, C.-H. Zhang, On tensor completion via nuclear norm minimization, *Foundations of Computational Mathematics* 16 (4) (2016) 1031–1068.
- [18] W. Cao, Y. Wang, J. Sun, D. Meng, C. Yang, A. Cichocki, Z. Xu, Total variation regularized tensor RPCA for background subtraction from compressive measurements, *IEEE Transactions on Image Processing* 25 (9) (2016) 4075–4090.
- [19] A. Anandkumar, P. Jain, Y. Shi, U. N. Niranjan, Tensor vs. matrix methods: Robust tensor decomposition under block sparse perturbations, in: *Artificial Intelligence and Statistics*, 2016, pp. 268–276.
- [20] C. Lu, J. Feng, Y. Chen, W. Liu, Z. Lin, S. Yan, Tensor robust principal component analysis: Exact recovery of corrupted low-rank tensors via convex optimization, in: *Proceedings of the IEEE conference on computer vision and pattern recognition*, 2016, pp. 5249–5257.

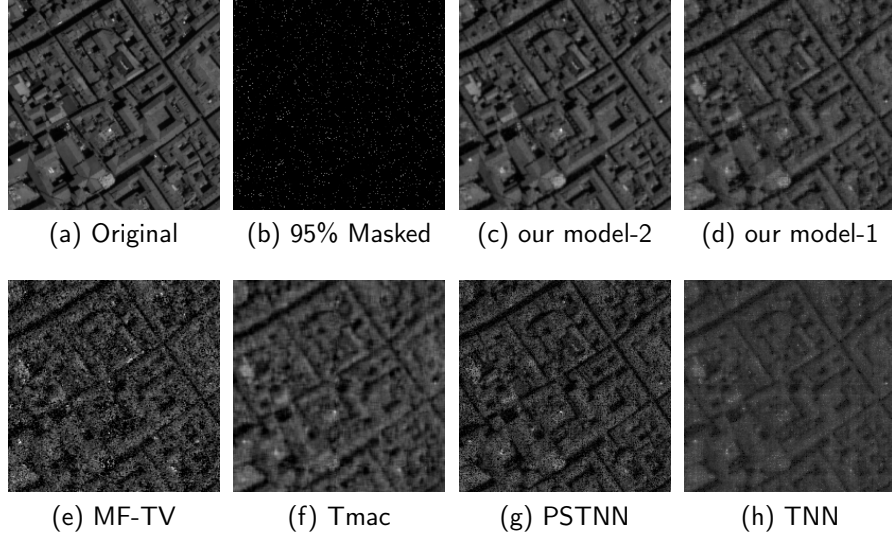


Figure 16: The image of the recovered HSI "Pavia" by our model-1 and model-2, MF-TV, Tmac, PSTNN and TNN. The sampling rates (SR) is 5%.

- [21] Z. Han, Y. Wang, Q. Zhao, D. Meng, L. Lin, Y. Tang, et al., A generalized model for robust tensor factorization with noise modeling by mixture of gaussians, *IEEE transactions on neural networks and learning systems* 29 (11) (2018) 5380–5393.
- [22] Z. Xu, F. Yan, Y. Qi, Bayesian nonparametric models for multiway data analysis, *IEEE transactions on pattern analysis and machine intelligence* 37 (2) (2013) 475–487.
- [23] Q. Zhao, L. Zhang, A. Cichocki, Bayesian cp factorization of incomplete tensors with automatic rank determination, *IEEE transactions on pattern analysis and machine intelligence* 37 (9) (2015) 1751–1763.
- [24] Y.-L. Chen, C.-T. Hsu, H.-Y. M. Liao, Simultaneous tensor decomposition and completion using factor priors, *IEEE transactions on pattern analysis and machine intelligence* 36 (3) (2013) 577–591.
- [25] Y.-L. Chen, C.-T. Hsu, H.-Y. M. Liao, Simultaneous tensor decomposition and completion using factor priors, *IEEE transactions on pattern analysis and machine intelligence* 36 (3) (2013) 577–591.
- [26] C. Lu, J. Feng, Y. Chen, W. Liu, Z. Lin, S. Yan, Tensor robust principal component analysis: Exact recovery of corrupted low-rank tensors via convex optimization, in: *Proceedings of the IEEE conference on computer vision and pattern recognition*, 2016, pp. 5249–5257.

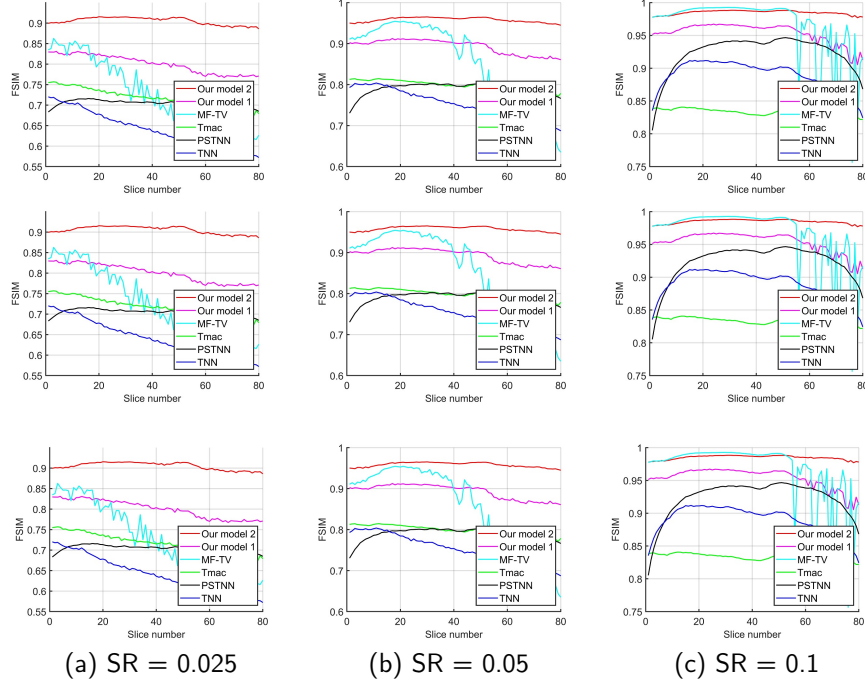


Figure 17: The PSNR, SSIM and FSIM of the recovered HSI "Pavia" by MF-TV, Tmac, TNN, PSTNN and our model-1 and model-2 for all bands, respectively.

- [27] O. Semerci, N. Hao, M. E. Kilmer, E. L. Miller, Tensor-based formulation and nuclear norm regularization for multienergy computed tomography, *IEEE Transactions on Image Processing* 23 (4) (2014) 1678–1693.
- [28] Z. Zhang, S. Aeron, Exact tensor completion using t-svd, *IEEE Transactions on Signal Processing* 65 (6) (2016) 1511–1526.
- [29] R. A. Harshman, M. E. Lundy, Parafac: Parallel factor analysis, *Computational Statistics & Data Analysis* 18 (1) (1994) 39–72.
- [30] L. R. Tucker, Some mathematical notes on three-mode factor analysis, *Psychometrika* 31 (3) (1966) 279–311.
- [31] W. Cao, Y. Wang, J. Sun, D. Meng, C. Yang, A. Cichocki, Z. Xu, Total variation regularized tensor rpca for background subtraction from compressive measurements, *IEEE Transactions on Image Processing* 25 (9) (2016) 4075–4090.
- [32] J. Liu, P. Musialski, P. Wonka, J. Ye, Tensor completion for estimating missing values in visual data, *IEEE transactions on pattern analysis and machine intelligence* 35 (1) (2012) 208–220.



- [33] S. Gandy, B. Recht, I. Yamada, Tensor completion and low-n-rank tensor recovery via convex optimization, *Inverse Problems* 27 (2) (2011) 025010.
- [34] R. Tomioka, K. Hayashi, H. Kashima, Estimation of low-rank tensors via convex optimization, *arXiv preprint arXiv:1010.0789*.
- [35] D. Goldfarb, Z. Qin, Robust low-rank tensor recovery: Models and algorithms, *SIAM Journal on Matrix Analysis and Applications* 35 (1) (2014) 225–253.
- [36] W. Cao, Y. Wang, C. Yang, X. Chang, Z. Han, Z. Xu, Folded-concave penalization approaches to tensor completion, *Neurocomputing* 152 (2015) 261–273.
- [37] Q. Zhao, D. Meng, X. Kong, Q. Xie, W. Cao, Y. Wang, Z. Xu, A novel sparsity measure for tensor recovery, in: *Proceedings of the IEEE International Conference on Computer Vision*, 2015, pp. 271–279.
- [38] J. Xue, Y. Zhao, W. Liao, J. C.-W. Chan, Nonconvex tensor rank minimization and its applications to tensor recovery, *Information Sciences* 503 (2019) 109–128.
- [39] M. E. Kilmer, K. Braman, N. Hao, R. C. Hoover, Third-order tensors as operators on matrices: A theoretical and computational framework with applications in imaging, *SIAM Journal on Matrix Analysis and Applications* 34 (1) (2013) 148–172.
- [40] T.-X. Jiang, T.-Z. Huang, X.-L. Zhao, L.-J. Deng, Multi-dimensional imaging data recovery via minimizing the partial sum of tubal nuclear norm, *Journal of Computational and Applied Mathematics* 372 (2020) 112680.
- [41] Y. Xu, R. Hao, W. Yin, Z. Su, Parallel matrix factorization for low-rank tensor completion, *arXiv preprint arXiv:1312.1254*.
- [42] J. Liu, P. Musialski, P. Wonka, J. Ye, Tensor completion for estimating missing values in visual data, *IEEE transactions on pattern analysis and machine intelligence* 35 (1) (2012) 208–220.
- [43] J. M. Bioucas-Dias, A. Plaza, N. Dobigeon, M. Parente, Q. Du, P. Gader, J. Chanussot, Hyperspectral unmixing overview: Geometrical, statistical, and sparse regression-based approaches, *IEEE journal of selected topics in applied earth observations and remote sensing* 5 (2) (2012) 354–379.
- [44] Y. Wang, J. Peng, Q. Zhao, Y. Leung, X.-L. Zhao, D. Meng, Hyperspectral image restoration via total variation regularized low-rank tensor decomposition, *IEEE Journal of Selected Topics in Applied Earth Observations and Remote Sensing* 11 (4) (2017) 1227–1243.
- [45] T.-Y. Ji, T.-Z. Huang, X.-L. Zhao, T.-H. Ma, G. Liu, Tensor completion using total variation and low-rank matrix factorization, *Information Sciences* 326 (2016) 243–257.

- [46] M. Razaviyayn, M. Hong, Z.-Q. Luo, A unified convergence analysis of block successive minimization methods for nonsmooth optimization, *SIAM Journal on Optimization* 23 (2) (2013) 1126–1153.
- [47] J.-F. Cai, E. J. Candès, Z. Shen, A singular value thresholding algorithm for matrix completion, *SIAM Journal on optimization* 20 (4) (2010) 1956–1982.
- [48] A. C. Sauve, A. O. Hero, W. L. Rogers, S. J. Wilderman, N. H. Clinthorne, 3d image reconstruction for a compton spect camera model, *IEEE Transactions on Nuclear Science* 46 (6) (1999) 2075–2084.
- [49] Y. Xu, W. Yin, Z. Wen, Y. Zhang, An alternating direction algorithm for matrix completion with nonnegative factors, *Frontiers of Mathematics in China* 7 (2) (2012) 365–384.
- [50] R. Glowinski, *Lectures on numerical methods for non-linear variational problems*, Springer Science & Business Media, 2008.
- [51] Q. Huynh-Thu, M. Ghanbari, Scope of validity of psnr in image/video quality assessment, *Electronics letters* 44 (13) (2008) 800–801.
- [52] Z. Wang, A. C. Bovik, H. R. Sheikh, E. P. Simoncelli, et al., Image quality assessment: from error visibility to structural similarity, *IEEE transactions on image processing* 13 (4) (2004) 600–612.
- [53] L. Zhang, L. Zhang, X. Mou, D. Zhang, FSIM: A feature similarity index for image quality assessment, *IEEE transactions on Image Processing* 20 (8) (2011) 2378–2386.
- [54] L. Wald, *Data fusion: definitions and architectures: fusion of images of different spatial resolutions*, Presses des MINES, 2002.
- [55] F. Kruse, A. Lefkoff, J. Dietz, Expert system-based mineral mapping in northern death valley, california/nevada, using the airborne visible/infrared imaging spectrometer (aviris), *Remote Sensing of Environment* 44 (2-3) (1993) 309–336.